



1 **A Coupled Ground Heat Flux-Surface Energy Balance Model of**
2 **Evaporation Using Thermal Remote Sensing Observations**

3 Devansh Desai^{1,11*}, Kaniska Mallick^{2,10*}, Bimal K. Bhattacharya³, Ganapati S. Bhat⁴, Ross
4 Morrison⁵, Jamie Clevery⁶, Will Woodgate⁷, Jason Beringer⁸, Kerry Cawse-Nicholson⁹, Siyan
5 Ma¹⁰, Joseph Verfaillie¹⁰, Dennis Baldocchi¹⁰
6

7 ¹Department of Physics, Electronics & Space Sciences, Gujarat University, Ahmedabad, India
8 ²Remote Sensing and Natural Resources Modeling, Department ERIN, Luxembourg Institute of
9 Science and Technology, Belvaux, L4422, Luxembourg
10 ³Agriculture & land Ecosystem Division, Space Applications Center, ISRO, Ahmedabad, India
11 ⁴Centre for Atmosphere and Oceanic Studies, Indian Institute of Sciences, Bengaluru, India
12 ⁵Centre for Ecology and Hydrology, Lancaster, UK
13 ⁶Terrestrial Ecosystem Research Network, College of Science and Engineering, James Cook
14 University, Cairns, Queensland
15 ⁷CSIRO Land and Water, Private Bag 5, Floreat 6913, Western Australia.
16 ⁸School of Earth and Environment (SEE), The University of Western Australia, WA, 6009,
17 Australia
18 ⁹Carbon Cycles and Ecosystems, Jet Propulsion Laboratory, California Institute of Technology,
19 United States
20 ¹⁰Environmental Science Policy and Management, University of California, Berkeley, United States
21 ¹¹Department of Physics, Institute of Science, Silver Oak University, Ahmedabad, Gujarat, India
22 *Corresponding authors:* Kaniska Mallick (kaniska.mallick@gmail.com) and Devansh Desai
23 (d-desai10793@gmail.com)

24
25
26
27
28
29
30



31 **Abstract**

32 The major undetermined problem in evaporation (ET) retrieval using thermal infrared (TIR)
33 remote sensing is the lack of a physically based ground heat flux (G) model and its amalgamation
34 with surface energy balance (SEB) model. Here, we present a novel approach based on coupling a
35 thermal inertia (TI)-based mechanistic G model with an analytical SEB model (Surface
36 Temperature Initiated Closure) (STIC, version STIC1.2). The coupled model is named as STIC-
37 TI and it uses noon-night land surface temperature (T_s), surface albedo and vegetation index from
38 MODIS Aqua in conjunction with a clear-sky net radiation model and ancillary meteorological
39 information. The SEB flux estimates from STIC-TI were evaluated with respect to the *in-situ*
40 fluxes from Eddy Covariance (EC) measurements in diverse agriculture and natural ecosystems of
41 contrasting aridity in the northern hemisphere (e.g., India, United States of America) and southern
42 hemisphere (e.g., Australia). Sensitivity analysis revealed substantial sensitivity of the STIC-TI
43 derived fluxes due to T_s uncertainty and partial compensation of sensitivity of G to T_s due to the
44 nature of the equations used in the TI-based G model. An evaluation of STIC-TI G estimates with
45 respect to *in-situ* measurements showed an error range of 12-21% across six flux tower sites in
46 both the hemispheres. A comparison of STIC-TI G estimates with other G models revealed
47 substantially better performance of the former. While the instantaneous noontime net radiation
48 (R_{Ni}) and latent heat flux (LE_i) was overestimated (15% and 25%), sensible heat flux (H_i) was
49 underestimated with error of 22%. The errors in G_i were associated with the errors in daytime T_s
50 and mismatch of footprint between the model estimates and measurements. Overestimation
51 (underestimation) of LE_i (H_i) was associated with the overestimation of net available energy (R_{Ni}
52 $- G_i$) and use of unclosed SEB measurements. Being independent of any leaf-scale conductance
53 parameterization and having a coupled sub-model of G, STIC-TI can make valuable contribution
54 to map and monitor water stress and evaporation in the terrestrial ecosystems using noon-night
55 thermal infrared observations from existing and future EO missions such as INSAT 4th generation
56 and TRISHNA.

57 **Keywords:** Thermal remote sensing, water stress, evaporation, ground heat flux, thermal inertia,
58 surface energy balance, STIC, terrestrial ecosystem



59 **1 Introduction**

60 Ground heat flux (G) is an intrinsic component of the surface energy balance (Sauer and Horton,
61 2005), affecting the net available energy for evaporation (ET) (the equivalent water depth of latent
62 heat flux, LE) and sensible heat flux. It represents an energy flow path that couples surface with
63 atmosphere and has important implications for the underlying thermal regime (Sauer and Horton,
64 2005). Evaporation is also an integral component of the surface energy balance where water is lost
65 from and within the soil-vegetation substrate complex through the ‘physics of evaporation and
66 ‘ecophysiology’ of transpiration while regulating the temperature and growth of vegetation (Martel
67 et al., 2018). Due to complex feedback between the physics of ground heat flux, land-atmosphere
68 interactions and vegetation ecophysiology, evaporation modelling at different space-time scales
69 remained a challenging task (Wang et al., 2013; Kiptala et al., 2013). This paper addresses the
70 challenge of simultaneous estimation of G and ET by combining thermal remote sensing
71 observations with a mechanistic G model and analytical surface energy balance (SEB) model.

72 Land surface temperature (LST or T_s) retrieved through thermal infrared (TIR) remote sensing
73 carries imprints of soil water content and is extraordinarily sensitive to evaporative cooling, which
74 makes it a crucial variable for estimating sensible heat flux (H) ET through the SEB models
75 (Kustas and Anderson, 2009; Mallick et al., 2014, 2015a, 2018a; Cammalleri and Vogt, 2015;
76 Anderson et al., 2012). However, it is the aerodynamic temperature (T_0) that is responsible for the
77 sensible heat transfer and the inequality of T_s versus T_0 introduces additional uncertainty in ET
78 retrieval through the SEB models. The differences between T_s and T_0 is accommodated either by
79 using two-source approximation of SEB (Anderson et al., 2012) or through an empirical extra-
80 resistance in the single-source SEB models (Su, 2002). In the SEB method, T_s represents the lower
81 boundary condition to estimate both sensible (H) and latent heat fluxes (LE) (Anderson et al.,
82 2012; Mallick et al., 2014, 2015a, 2018a). SEB models mainly emphasize on estimating H by
83 resolving the aerodynamic conductance (g_A) and resolves LE as a residual SEB component as
84 follows:

$$LE = R_N - G - H \quad (1)$$

85 R_N is the net radiation. The proportion of R_N that is partitioned into conductive heat flux (G)
86 depends upon soil properties like its albedo, soil moisture, soil thermal properties such as heat



87 conductance and capacity, which vary with mineral, organic and water fractions. The magnitude
88 of G varies greatly across different ecosystems from as low as $< 20 \text{ W m}^{-2}$ under dense forest to as
89 high as 100 W m^{-2} over dry soils in arid and semi-arid landscapes or the rows between crops. In
90 the humid ecosystems with predominantly dense canopies and high mean fractional vegetation
91 cover, G contributes to a small proportion in eq. (1). Dense canopy cover leads to less transmission
92 of downwelling shortwave radiation flux through multiple layers of canopies, which results in low
93 warming of the soil floor. Due to persistently high soil water content, humid ecosystems generally
94 show low diurnal and seasonal variability in G . By contrast, the magnitude of G is substantially
95 large in the arid and semi-arid ecosystems with sparse and open canopy and high water stress. One
96 of the outstanding challenges in SEB modeling concerns an accurate estimation of G in the open
97 canopy system such as savanna with mixed vegetation or in ecosystems with low mean fractional
98 vegetation cover, predominant water stress, and strong seasonality in soil moisture.

99 While the utility of a surface heat capacity and thermal inertia (TI)-based mechanistic G model
100 was demonstrated by Murray and Verhoef (2007), Verhoef et al. (2012), and Mallick et al. (2015b);
101 the potential of an analytical SEB model (Mallick et al., 2014, 2015, 2016, 2018a,b) for mapping
102 ET in a variety of ecological transects was also demonstrated by Bhattarai et al. (2018, 2019).
103 Recognizing the significant conclusions of Verhoef et al. (2012), Mallick et al. (2014; 2015a,b;
104 2016; 2018a,b) and Bhattarai et al. (2018, 2019), there is a need to overcome the challenges of
105 accurate G estimation and to complement the overarching gaps in SEB modeling in the sparsely
106 vegetated open canopy systems. Present study coupled the TI-based G model of Murray and
107 Verhoef (2007), after required modification, with the current version of an analytical ET model,
108 the Surface Temperature Initiated Closure (STIC, version 1.2; Mallick et al., 2014, 2015a, 2016,
109 2018a,b) and evaluated this new coupled G -SEB model in different ecosystems of contrasting
110 aridity.

111 Remote sensing-based ET models generally use linear and non-linear relationships for estimating
112 G and such methods generally employ R_N , T_s , albedo (α_R), and NDVI (e.g., Bastiaanssen et al.,
113 1998; Friedl, 2002; Santanello and Friedl, 2003). While the inclusion of T_s and albedo serves as a
114 proxy for soil moisture and surface characteristics effects in G , inclusion of NDVI provides a
115 scaling of $G - R_N$ ratio for different fractional vegetation cover. Unfortunately, all the approaches
116 are empirical and do not include any information of deep soil temperature or daily temperature



117 amplitude as lower boundary conditions. These empirical model functions also lack the universal
118 consensus. Setting G as a fraction of R_N does not solve the energy balance equation and disregards
119 the role of thermal inertia of the land surface (Mallick et al., 2015b). This could introduce
120 substantial uncertainty in LE estimation because G effectively couples the surface energy balance
121 with energy transfer processes in the soil thermal regime. It provides physical feedback to LE
122 through the effects of soil moisture, temperature, and conductivity (thermal and hydraulic) (Sauer
123 and Horton, 2005). Such feedbacks are most critical in the arid and semi-arid ecosystems where
124 LE is significantly constrained by the soil moisture dry-down. The limits imposed on LE by the
125 water stress consequently result in greater partitioning of the net available energy (i.e., $R_N - G$)
126 into H and G (Castelli et al., 1999).

127 When LE is reduced due to soil moisture dry-down and water stress, both G and T_s tend to show
128 rapid rise. Therefore, the surface energy balance equation could be linked with mechanistic G
129 model, T_s harmonics (Verhoef, 2004), and soil moisture availability. Realizing the importance of
130 direct estimates of G in LE and invigorated by the advent of TIR remote sensing, Verhoef et al.,
131 (2012) demonstrated the potential of a TI-based mechanistic model (Murray and Verhoef, 2007)
132 (MV2007 hereafter) for spatio-temporal G estimates in the semi-arid ecosystems of Africa. Some
133 studies also emphasized the importance of using day-night T_s and R_N for estimating G (Mallick et
134 al., 2015b; Bennet et al., 2008; Tsuang, 2005). The method of MV2007 has so far been tested in a
135 stand-alone mode, and no remote sensing method is so far attempted to combine such a mechanistic
136 G model (e.g., MV2007-TI model) with a SEB model for coupled energy-water flux estimation
137 and validation.

138 By integrating T_s into a combined structure of the Penman-Monteith (PM) and Shuttleworth-
139 Wallace (SW) model, an analytical SEB modeling was proposed by Mallick et al., (2014, 2015a,
140 2016). The model, Surface Temperature Initiated Closure (STIC), is based on finding analytical
141 solution for aerodynamic and canopy-surface conductance (g_A and g_S) where the expressions of
142 the conductances were constrained with an aggregated water stress factor. Through physically
143 linking water stress (T_s derived) with g_A and g_S , STIC established a direct feedback between T_s ,
144 H and LE, and simultaneously overcame the need of empirical parameterization for estimating the
145 conductances (Mallick et al., 2016, 2018a). Different versions of STIC have been extensively
146 validated in different ecological transects (Tropical rainforest to woody savanna) and aridity



147 gradients (humid to arid) (Trebs et al., 2021; Bai et al., 2021; Mallick et al., 2015a; 2016; 2018a,
148 b; Bhattarai et al., 2018, 2019). Realizing the significance of mechanistic G model (MV2007) and
149 the advantage of analytical solution for different turbulent heat fluxes and conductances from the
150 STIC model, this paper presents the first-ever coupled implementation of MV2007 G with the
151 most recent version of STIC (STIC1.2). We name this new coupled model as STIC-TI and it
152 requires day-night T_s and associated remotely sensed land surface variables as inputs. We
153 performed subsequent evaluation of STIC-TI in nine terrestrial ecosystems in arid, semi-arid and
154 sub-humid climate in India, the United States of America (USA) (representing northern
155 hemisphere) and Australia (representing southern hemisphere) at the eddy covariance flux tower
156 sites. The current study addresses the following research questions and objectives:

157 (i) What is the performance of STIC-TI G estimates when compared with contemporary empirical
158 models in ecosystems having low mean fractional vegetation cover (f_c) (≤ 0.5) and having larger
159 soil exposure to radiation for example in Savanna?

160 (ii) How do the estimates from STIC-TI LE and H fluxes compare with LE and H observations in
161 diverse terrestrial ecosystems that represent a varied range of f_c (0.25 – 0.5) covering cropland,
162 savanna, mulga vegetation spread across arid, semi-arid, sub-humid, humid climates over a vast
163 range of rainfall (250 to 1730 mm), temperature (-4 to 46°C) and soil regimes?

164 (iii) What is the seasonal variability of G and evaporative fraction from STIC-TI model in a wide
165 range of ecosystems having contrasting aridity and vegetation cover?

166 It is important to mention that assessing the performance of STIC-TI LE and H with respect to
167 other SEB models is not within the scope of the present study. The prime focus of the current study
168 is to assess the sensitivity of STIC-TI, temporal variability of the retrieved SEB fluxes, and cross-
169 site validation of the individual SEB components.

170 A list of variables, their symbols and corresponding units are given in Table A1 in Appendix A.

171 **2 Study area and datasets**

172 **2.1 Study site characteristics**

173 The present study was conducted at nine flux tower sites (four sites in India; three sites in Australia;
174 two sites in USA) equipped with Eddy Covariance (EC) measurement systems. The distribution



175 of the flux tower sites considered for the present study are shown in Fig. 1 below. The sites cover
176 a wide range of climate, vegetation types, low fractional vegetation cover (f_c) of around 0.5 and
177 have contrasting aridity (Table 1). In India, a network of EC towers was set up under Indo-UK
178 INCOMPASS (Interaction of Convective Organization and Monsoon Precipitation, Atmosphere,
179 Surface and Sea) Program (Turner et al., 2019) at Jaisalmer (IND-Jai) in Rajasthan state, Nawagam
180 (IND-Naw) in Gujarat state, Samastipur (IND-Sam) in Bihar state and under Newton-Bhaba
181 programme (Morisson et al., 2019 a,b) at Dharwad (IND-Dha) in Karnataka state. The fetch ratio
182 of EC towers in India varied from 1:50 to 1:100 representing 90% of fetch area. The mean annual
183 f_c was found to vary from 0.25 to 0.52 with standard deviation (SD) ranging from 0.1 to 0.16.
184 The IND-Jai site represents arid western zone over desert plains of natural grassland ecosystem.
185 The region receives very low rainfall (100 – 300 mm) during monsoon and experiences a wide
186 range in air temperature, high solar radiation, wind speed and high evaporative demand (Raja et
187 al., 2015). The IND-Naw site represents semi-arid agroecosystem in the middle Gujarat agro-
188 climatic zone of north-west India and has a pre-dominant rice-wheat cropping system. The IND-
189 Sam site has sub-humid climate of north-west alluvial plain zone in the Indo-Gangetic Plain (IGP)
190 situated in the eastern India and this site also follows rice-wheat crop rotation. IND-Dha represents
191 humid sub-tropical climate of transition zone in the southern India and this site comprises of crops.

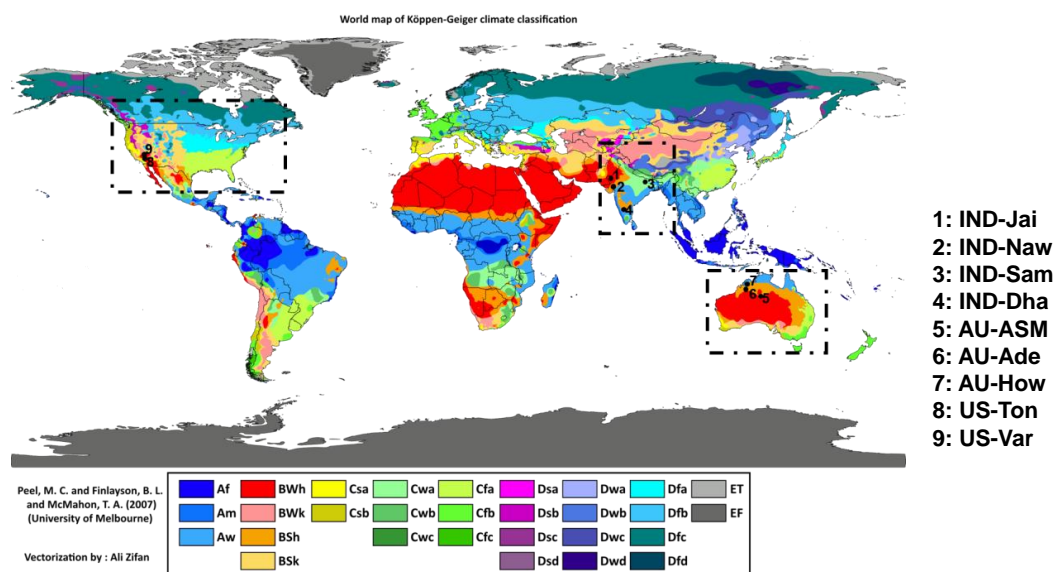




Figure 1: Locations of the flux tower sites in India, Australia and USA overlaid on climate type map. (Image Source: By Peel, M. C., Finlayson, B. L., and McMahon, T. A. (University of Melbourne) enhanced, modified, and vectorized by Ali Zifan; Hydrology and Earth System Sciences: "Updated world map of the Köppen-Geiger climate classification" (Supplement) map in PDF (Institute for Veterinary Public Health). Legend explanation, CC BY-SA 4.0, <https://commons.wikimedia.org/w/index.php?curid=47086879>)

192 In USA, two EC tower sites were located at Tonzi Ranch (US-Ton) and Vaira Ranch (US-Var), in
193 the lower foothills of the Sierra Nevada Mountains. Both the EC stations are part of the
194 AMERIFLUX Management Project (<https://ameriflux.lbl.gov/>). US-Ton is classified as an oak
195 savanna woodland on privately owned land. While the overstorey is dominated by blue oak trees
196 (40% of total vegetation) with intermittent grey pine trees (3 trees ha⁻¹), the understory species
197 include a variety of grasses and herbs. The mean annual rainfall at this site is 559 mm. US-Var is
198 a grassland dominated site and the growing season is confined to the wet season only, typically
199 from October to early May. The mean annual rainfall at this site is 559 mm. The mean annual f_c
200 was found to vary from 0.18 to 0.26 and SD of the order of 0.06 to 0.07.

201 In Australia, three EC tower sites were located at Howard Springs (AU-How), Alice Springs
202 Mulga (AU-ASM), Adelaide river (AU-Ade) in the Northern Territory as part of the OzFlux
203 network (Beringer et al., 2016) and the Terrestrial Ecosystem Research Network (TERN), which
204 is supported by the National Collaborative Infrastructure Strategy (NCRIS)
205 (<http://www.ozflux.org.au/monitoringsites/index.html>). The AU-How is situated in the Black
206 Jungle Conservation Reserve representing an open woodland savanna and the mean annual rainfall
207 is 1750 mm. The AU-ASM is located on Pine Hill cattle station near Alice Springs. The woodland
208 is characterized by mulga canopy and mean annual rainfall is 306 mm. AU-Ade represents savanna
209 with a mean annual rainfall of 1730 mm. The mean annual f_c varied from 0.21 to 0.48 having SD
210 range of 0.08 - 0.17. A description of Australian flux sites is given in Beringer et al. (2016).

211
212
213
214
215
216
217
218



219 **Table 1:** An overview of the EC flux tower site characteristics in the present study

Hemisphere	Sites	Latitude (°N), Longitude (°E)	Climate & Vegetation	Mean f_c (SD)	Soil texture	T _A range (°C)	Mean Annual P (mm)	Observation period
Northern	Jaisalmer (IND-Jai)	26.99, 71.34	Arid grassland	0.25(±0.1)	Loamy fine sand to coarse sand	8 – 40	250	2017 – 2018
	Nawagam (IND-Naw)	22.80, 72.57	Semi-arid cropland	0.41(±0.13)	Sandy loam	9 – 39	700	2017 – 2018
	Samastipur (IND-Sam)	26.00, 85.67	Humid subtropical cropland	0.52(±0.16)	Sandy loam to loam	10 – 39	1000	2017 – 2018
	Dharwad (IND-Dha)	15.50, 74.99	Tropical Savanna	0.36(±0.11)	Shallow to medium black clay and red sandy loam soils	12 – 40	650	2016 – 2018
	Tonzi ranch (US-Ton)	38.43, -120.96	Woody Savanna	0.18(±0.06)	Red sandy clay loam	0 – 40	559	2011 – 2019
	Vaira ranch (US-Var)	38.41, -120.95	Arid grassland	0.26(±0.07)	Rocky silt loam	0 – 40	559	2011 – 2019
Southern	Alice Springs Mulga (AU-ASM)	22.28, 133.24	Semi-arid mulga	0.21(±0.09)	Loamy sand	(-4) – 40	305	2011 – 2014
	Howard Springs (AU-How)	12.49, 131.15	Tropical savanna	0.48(±0.17)	Red kandasol	19 – 34	1700	2011 – 2014
	Adelaide River (AU-Ade)	13.07, 131.11	Savanna	0.42(±0.08)	Yellow hydrosol, shallow, loamy sand with coarse gravel	16 – 37	1730	2007 – 2009

220 T_A: Air temperature during the observation period; P: rainfall (mm) measured using rain gauge at flux tower site during the study
 221 period. IND is for India, AU is for Australia, and US is for the United States; SD is standard deviation of annual mean f_c which is
 222 computed from NDVI as mentioned in section 3.1.

223



224 2.2 Datasets

225 2.2.1 Micrometeorological data at flux tower sites

226 Standardized, controlled and harmonized surface energy balance (SEB) flux and meteorological
227 data from nine EC towers were used in the present analysis. In Australia, the SEB measurements
228 were carried out at varying heights of 15 m, 23 m and 11.6 m at AU-Ade, AU-How and AU-ASM,
229 respectively. In India, the EC measurement height was maintained approximately at 8 m above the
230 surface, except at IND-Dha where it was installed at a height of 4.2 m. In USA, the SEB
231 measurements were carried out at tower heights of 23 m at US-Ton and 2 m US-Var. A summary
232 of the instrumentation is given in Table A2 of appendix A. All the flux tower sites were equipped
233 with a range of meteorological instrumentation which measured diurnal air temperature (T_A) and
234 relative humidity (R_H), four components of the net radiation (R_N , consisting of down- and up-
235 welling shortwave and long-wave radiation (SW_{\downarrow} , SW_{\uparrow} , LW_{\uparrow} and LW_{\downarrow} , respectively)) above the
236 vegetated canopy. In addition, the diurnal soil heat flux (G) and soil temperature (T_{ST}) were
237 measured at all the three Australian sites and two US sites. In India, the diurnal soil heat flux was
238 measured only at IND-Dha.

239 For the Indian sites, the raw EC measurements of the turbulent wind vectors (u , v and w , for
240 horizontal, meridional and vertical, respectively), sonic temperature (T), and CO_2 and water vapor
241 mass density were recorded at a sampling rate of 20 Hz. Raw EC data were post-processed to
242 obtain level-3 quality controlled and harmonized surface fluxes at 30-minute flux averaging
243 intervals using EddyPRO® Flux Calculation Software (LI-COR Biosciences, Lincoln, Nebraska,
244 USA) using the data handling protocol described by Bhat et al. (2019). The EC data from the
245 OzFlux sites was averaged over 30 minutes recorded by the logger and processed through levels
246 using the PyFluxPro standard software processing scripts as mentioned in Isaac et al. (2017). The
247 Level 3 (L3) used in this paper was produced using PyFluxPro (Isaac et al., 2017) employing the
248 Dynamic INtegrated Gap filling and partitioning for Ozflux (DINGO) system as described in
249 Donohue et al. (2014) and Beringer et al. (2016). The quality checked EC data at 30 minute
250 intervals for two AMERIFLUX sites US-Ton and US-Var was acquired from
251 <https://doi.org/10.17190/AMF/1245971> & <https://doi.org/10.17190/AMF/1245984>, respectively.



252 **2.2.2 Remote sensing data**

253 Optical and thermal remote sensing observations available from Moderate Resolution Imaging
 254 Spectroradiometer (MODIS) (Didan et al., 2015) on-board Aqua platform were used in the present
 255 analysis (Table 2) for estimating G and associated SEB fluxes. These include land surface products
 256 (eight-day) of noon-night land surface temperature (LST or T_s) and surface emissivity (ϵ_s)
 257 (MYD11A2), daily surface albedo (α_R) (MCD43A3), 16-day NDVI (MYD13A2). The overpass
 258 times of MODIS Aqua are at 1:30 pm and 1:30 am (IST). The noon-night pair of thermal remote
 259 sensing observations from Aqua are close to time of occurrences of maximum and minimum soil
 260 surface temperature (see Figure 2) and are therefore ideal for soil heat flux modeling using thermal
 261 inertia. The MODIS Terra overpass times are at 11 AM and 11 PM and are quite away from time
 262 of occurrences of minimum-maximum soil temperatures. Therefore, MODIS Aqua acquisition
 263 times were used.

264 **Table 2:** A summary of MODIS Aqua optical and thermal remote sensing products used in the
 265 present study

Data type	Product ID (version)	Variables used	Spatial resolution (m)	Temporal resolution	Purpose	Inputs to equation numbers
Land surface temperature and emissivity	MYD11A2 (V006)	T_s and ϵ_s	923	8-day	For estimating R_{Ni} , G_i , LE_i , H_i	(5), (13), (C6), (C7), (B8)
Surface albedo	MCD43A3 (V006)	α_R	462	8-day composite from daily	For estimating R_{Ni} , G_i	(5), (B3)
Vegetation index	MYD13Q1 (V006)	NDVI	250	16-day	For estimating G_i	(4)

266 The key variables of SEB modeling such as LST and ϵ_s , were retrieved at 923m spatial resolution
 267 from MODIS Aqua noon-night thermal infrared (TIR) observations (MYD11A2) in bands 11.03
 268 μm and 12.02 μm using a generalized split-window algorithm by Wan et al., (2015). The land



269 surface emissivity was estimated from land cover types, atmospheric column water vapor and
270 lower boundary air surface temperature that are separated into tractable sub-ranges for optimal
271 retrieval. The albedo was estimated from MODIS (MCD43A2 Version 6) Bidirectional
272 Reflectance Distribution Function and Albedo (BRDF/Albedo) daily dataset (Schaaf et al., (2002))
273 at 462 m spatial resolution. Eight-day compositing for albedo was done from daily products
274 (MYD11A2). NDVI was estimated from MODIS Vegetation Indices (MYD13Q1) Version 6 data
275 and are generated every 16-day at 250 meter (m) spatial resolution as a Level 3 product.
276 MYD13Q1 contains Normalized Difference Vegetation Index (NDVI) and Enhanced Vegetation
277 Index (EVI). In the present study, NDVI has been used because of its universal applicability (Xue
278 and Su, 2017; Drori et al. 2020; Bhandari et al., 2012). All the input remote sensing variables
279 mentioned in table 2 are resampled to spatial resolution of MYD11A2 (V006) product (923 m).

280 **3 Methodology**

281 **3.1 Coupled soil heat flux-SEB model**

282 In this paper, we modified a thermal inertia (TI) based soil heat flux (G) model using noon-night
283 thermal remote sensing observations and thereafter coupled the TI-based G with STIC1.2. A clear-
284 sky net radiation (R_N) model was also introduced into this coupled model and R_N estimation
285 algorithm is described in Appendix B. The estimation of G through modifying MV2007-TI
286 approach and its coupling with STIC1.2 is the most novel component of the modeling scheme, and
287 it is therefore described in the main body of the paper (section 3.1.1). Such a coupling enabled the
288 implementation of a mechanistic G model along with an analytical SEB model using optical-
289 thermal remote sensing data. The coupled model is hereafter referred as STIC-TI. The noteworthy
290 features of STIC-TI are: (1) estimating G by modifying the mechanistic MV2007-TI model using
291 noon-night T_s data from thermal remote sensing observations available through polar orbiting
292 satellite platform (e.g. MODIS Aqua), (2) coupling MV2007-TI G model with STIC1.2 to
293 simultaneously estimate surface moisture availability (M), G, and SEB fluxes, (3) introducing
294 moisture availability information in G to better constrain the aerodynamic and canopy-surface
295 conductances as well as the SEB fluxes, (4) the G model uses fundamental soil physical properties,
296 moisture constants and soil texture that majorly influence soil heat conduction, (5) derivation of
297 amplitude of ecosystem-scale surface soil temperature (from top soil to 0.1 m soil depth).



298 **3.1.1 MV2007 soil heat flux model based on Thermal Inertia (TI)**

299 The functional form for estimating instantaneous G (G_i , hereafter) (eq. 2 below) is based on the
300 harmonic analysis of soil surface temperature and is described in detail by Murray and Verhoef
301 (2007) and Maltese et al. (2013).

$$G_i = \Gamma \left[(1 - 0.5f_c) \left(\sum_{n=1}^k A\sqrt{n}\omega \sin \left(n\omega t + \phi'_n + \frac{\pi}{4} - \frac{\pi\Delta t}{12} \right) \right) \right] = \Gamma J_s \quad (2)$$

302 G_i is the soil heat flux at the surface at a particular instance (W m^{-2}), Γ is the soil thermal inertia
303 ($\text{J m}^{-2} \text{K}^{-1} \text{s}^{-0.5}$), k is the total number of harmonics used, A is the amplitude ($^{\circ}\text{C}$) of the n^{th} soil
304 surface temperature (T_{ST}) harmonic, ω is the angular frequency (rads^{-1}), t is the time (s), ϕ'_n is the
305 phase shift of the n^{th} soil surface temperature harmonic (rad), J_s is the summation of harmonic
306 terms of soil surface temperature (K), and Δt (s) is time offset between the canopy composite
307 temperature and the below-canopy soil surface temperature. Here, we represent G_i and A as
308 ecosystem-scale ($\leq 1\text{km}$) soil heat flux and surface soil temperature amplitude (within 0.1 m from
309 the soil top), respectively and assume it to be valid for different vegetated landscape.

310 Since we have considered a single pair (noon-night corresponding to 1 pm and 1 am) of MODIS
311 aqua LST data in the present study, the phase shift (ϕ'_n) is taken as zero and number of harmonics
312 is taken as one ($k=1$) for estimating noontime G_i . Thus equation (2) is modified as follows:

$$G_i = \Gamma \left[(1 - 0.5f_c) \left(A\sqrt{\omega} \sin \left(\omega t' + \frac{\pi}{4} - \frac{\pi\Delta t}{12} \right) \right) \right] = \Gamma J_s \quad (3)$$

313 Δt (s) is found to be 1.5 h (Murray and Verhoef, 2007). With the two boundary values (i.e., $\Delta t=1.5$
314 h for $f_c = 1$ and $\Delta t = 0$ for $f_c = 0$), a linear approach is proposed here to describe the time offset Δt
315 as a function of vegetation fraction (f_c) (Murray and Verhoef, 2007; Maltese et al., 2013). The f_c
316 was derived from NDVI on a given day or period and its practically occurring upper-lower limits
317 obtained from annual cycle.

318
319



$$\Delta t = 1.5 f_c \quad (4)$$

320 ***3.1.1.1 Scaling function for estimating ecosystem-scale surface soil temperature amplitude (A)***

321 Estimating ecosystem-scale A involves two steps, (a) computing point-scale soil surface
322 temperature amplitude (from surface to 0.1m depth) (T_{STA} , hereafter) from the available
323 measurements of soil surface temperature, and (b) linking T_{STA} with remote sensing variables to
324 develop scaling functions for A.

325 Several studies suggested theoretical sinusoidal trajectory of soil surface and sub-surface
326 temperatures (Gao et al., 2010), where the amplitude is maximum at the surface and it gradually
327 decreases with depth to become close to zero until the damping depth where soil temperature is
328 almost invariant through day-night called deep soil temperature. However, the diurnal surface soil
329 temperature measurements (within top 0.1 m depth) across different flux tower sites showed a
330 sinusoidal-exponential behavior, i.e. sinusoidal pattern from sunrise until the afternoon and
331 exponential pattern from afternoon through sunset to the next sunrise. An illustrative example of
332 the theoretical and observed trajectories of surface soil temperature is shown in Fig. 2. This diurnal
333 surface soil temperature variation has a single harmonic component (Gao et al., 2010). For
334 computing T_{STA} , theoretical half-curve of sinusoidal pattern is assumed and was derived from
335 measurements as exemplified in Fig 2.

336

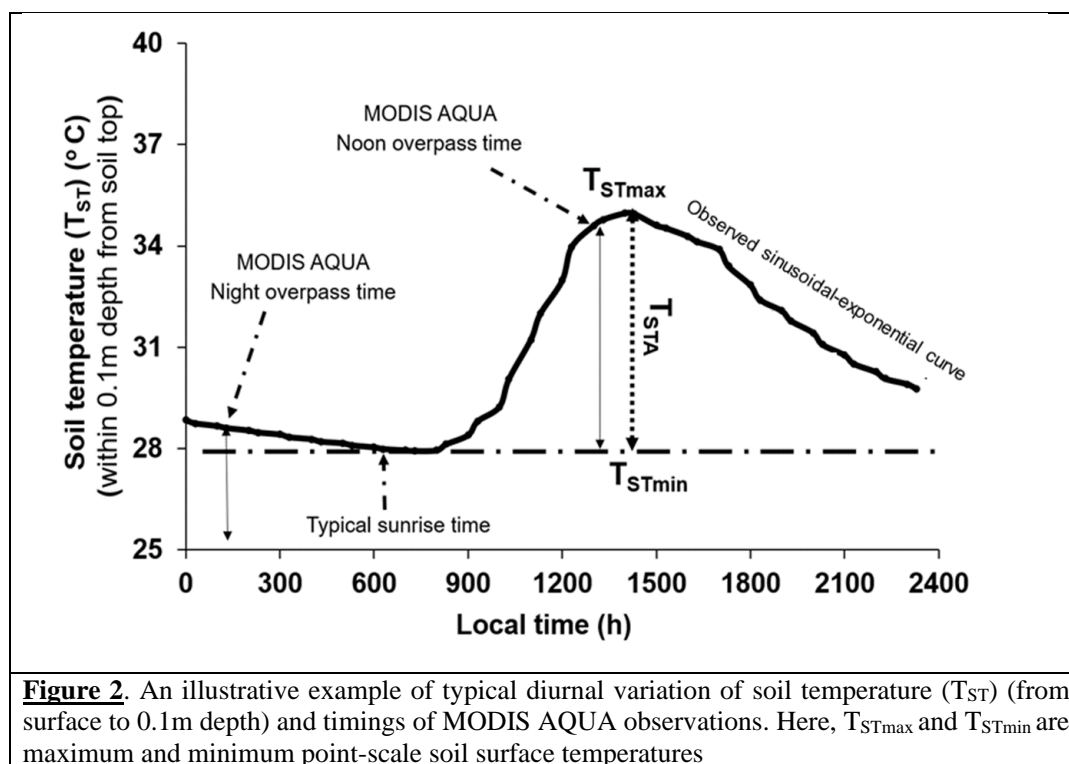


Figure 2. An illustrative example of typical diurnal variation of soil temperature (T_{ST}) (from surface to 0.1m depth) and timings of MODIS AQUA observations. Here, T_{STmax} and T_{STmin} are maximum and minimum point-scale soil surface temperatures

337

338 It is evident from Fig. 2 that T_{STmin} represents minimum surface soil temperature occurring 1-1.5
339 h after sunrise and T_{STmax} occurs during 12.30 – 15.00 h local time. T_{STmin} is thus close to deep soil
340 temperature as well as minimum soil temperature of other sub-surface soil layers. Both T_{STmin} and
341 T_{STmax} represent lower and upper limits of surface soil temperature on a given day and also lower
342 and upper boundary conditions of soil heat flux conducting through topsoil at noontime. The *in-*
343 *situ* measured T_{ST} on completely clear-sky days at OzFlux sites were used to extract T_{STmax} and
344 T_{STmin} . The T_{STA} was derived as the difference between T_{STmax} and T_{STmin} from the theoretical half-
345 curve of sinusoidal pattern.

346 T_{STA} is generally influenced by several land surface characteristics such as surface temperature
347 and surface albedo of soil-canopy complex, surface heat capacities, fractional canopy cover and
348 thermal conductivity (White, 2013). T_S and α_R are the major thermal and reflective land surface
349 properties that have strong synergy with surface soil temperature dynamics. Hence, we have used
350 bivariate regression analysis to develop a scaling function for estimating ecosystem-scale T_{STA}
351 (top to 0.1m depth). The bivariate regression is based on the difference of noon (d) and night (n)



352 T_S data and α_R (Duan et al., 2013, Li Tian et al., 2014) from MODIS Aqua. The scaling function
353 given in eq. (5) estimates ecosystem-scale T_{STA} (symbolized as ‘A’ in equation 5) from surface to
354 0.1 m soil depth:

$$A = B_1(T_{Sd} - T_{Sn}) + B_2(\alpha_R) + B_3 \quad (5)$$

355 Here, B_1 , B_2 , B_3 are coefficients of regression model; T_{Sd} and T_{Sn} are noon and nighttime LST,
356 respectively. The results of this regression analysis are elaborated in section 4.1.

357 **3.1.1.2 Estimating Γ**

358 Γ is the key variable for estimating G_i using eq. (2). MV2007 adopted the concept of normalized
359 thermal conductivity (Johansen, 1975) and developed a physical method to estimate Γ as follows:

$$\Gamma = e^{[Y'(1 - S_r^{(Y' - \delta)})]}(\tau_* - \tau_0) + \tau_0 \quad (6)$$

360 where τ_* and τ_0 are the thermal inertia for saturated and air-dry soil ($J m^{-2} K^{-1} s^{-0.5}$); $\tau_0 = D_1\theta^* + D_2$;
361 $\tau_* = D_3 (\theta^{*-1.29})$; Y' (–) is a parameter depending on the soil texture (Murray and Verhoef, 2007;
362 Minasny, 2007; Anderson et al., 2007); $S_r (m^3 m^{-3})$ is relative saturation and is equal to (θ/θ^*) ; δ
363 (unitless) is the shape parameter which is dependent on the soil texture. $\theta^* (m^3 m^{-3})$ is the soil
364 porosity (equal to the saturated soil moisture content when soil moisture suction is zero), $\theta (cm^3$
365 $cm^{-3})$ is the volumetric soil moisture and D_1 , D_2 , D_3 are coefficients which were derived from a
366 large number of experimental data. The reported global values of D_1 , D_2 , and D_3 were taken as -
367 1062.4, 1010.8, 788.2, respectively (Maltese et al., 2013). The value for θ^* and shape parameter
368 for soil textures across study sites were specified according to Van Genuchten et al. (1980). The
369 details are mentioned in Table E1 of Appendix E.

370 In the present study, the relative soil moisture saturation, $S_r (\theta/\theta^*)$ is represented in terms of an
371 aggregated moisture availability (M) of canopy-soil complex through a linear function (eq. 12). In
372 case of zero canopy cover, M represents the soil moisture availability from surface to 0.1 m depth.
373 In sparse and open canopy, rates of moisture availability from soil to root and root to canopy were
374 assumed same.



375 Theoretically, M is expressed as available soil moisture fraction between field capacity (θ_{fc}) and
376 permanent wilting (θ_{wp}) point as given in eq. (7) below.

$$M = \frac{\theta - \theta_{wp}}{\theta_{fc} - \theta_{wp}} \quad (7)$$

377 Where, θ_{fc} ($\text{m}^3 \text{m}^{-3}$) is the volumetric soil moisture at the field capacity (at a suction of 330 hpa)
378 and θ_{wp} ($\text{m}^3 \text{m}^{-3}$) is the volumetric soil moisture at the permanent wilting point (at suction of 15000
379 hpa) (Singh, 2007). Since θ_{fc} , θ_* , θ_{wp} are soil moisture constants and depends on the soil texture,
380 dividing the numerator and denominator in eq. (7) by θ_* gives the following expression:

$$M = \frac{\frac{\theta}{\theta_*} - \frac{\theta_{wp}}{\theta_*}}{\frac{\theta_{fc}}{\theta_*} - \frac{\theta_{wp}}{\theta_*}} \quad (8)$$

381 Due to their dependence on soil texture, the ratios (θ_{fc}/θ_*) and (θ_{wp}/θ_*) are treated as constants.
382 These are represented as C and C' in the later equations (eq. 9, 10, and 11). The constants, C and
383 C' vary from 0.3 to 0.8 and from 0.1 to 0.4 (Murray and Verhoef, 2007; Minasny et al., 2011;
384 Anderson et al., 2007), respectively over different soil textures.

$$M = \frac{\frac{\theta}{\theta_*} - C'}{C - C'} \quad (9)$$

$$M(C - C') = \left(\frac{\theta}{\theta_*}\right) - C' \quad (10)$$

385 By replacing S_r in eq. (6) as θ/θ_* and by rearranging eq. (10), the following linear function is
386 obtained.

$$S_r = \frac{\theta}{\theta_*} = M(C - C') + C' = M' \quad (11)$$

387 Thus, the modified equation to calculate Γ is given by eq. (12) as follows:

$$\Gamma = e^{\left[Y'(1 - M'(Y' - \delta))\right]}(\tau_* - \tau_0) + \tau_0 \quad (12)$$



388 By substituting the values obtained from eq. (4), (5) and (12) into eq. (3), we obtained the
389 instantaneous ecosystem-scale G_i corresponding to MODIS Aqua noontime overpass. The intrinsic
390 link between G_i estimates through MV2007-TI and SEB scheme in STIC1.2 is made through M ,
391 where the computation of M follows the procedure as described in Mallick et al. (2016, 2018a, b)
392 and Bhattarai et al. (2018). (description in Appendix C).

393 **3.1.1.3 Estimating M**

394 In STIC1.2, an aggregated moisture availability (M) of canopy-soil complex is expressed as the
395 ratio of the ‘vapor pressure difference’ between the aerodynamic roughness height of the canopy
396 (i.e., source/sink height) and air to the ‘vapor pressure deficit’ between aerodynamic roughness
397 height to the atmosphere:

$$M = \frac{(e_0 - e_A)}{(e_0^* - e_A)} = \frac{(e_0 - e_A)}{\kappa(e_S^* - e_A)} = \frac{s_1(T_{0D} - T_D)}{\kappa s_2(T_S - T_D)} \quad (13)$$

398 Where e_0 and e_0^* are the actual and saturation vapor pressure at the source/sink height; e_A is the
399 atmospheric vapor pressure; e_S^* is the saturation vapor pressure at the surface; T_{0D} is dew point
400 temperature at the source/sink height; T_S is the LST; T_D is the air dew point temperature; s_1 and s_2
401 are the psychrometric slopes of the saturation vapor pressure and temperature between $(T_{0D} - T_D)$
402 versus $(e_0 - e_A)$ and $(T_S - T_D)$ versus $(e_S^* - e_A)$ relationship; and κ is the ratio between $(e_0^* - e_A)$
403 and $(e_S^* - e_A)$. To solve the eq. (13), estimation of T_{0D} is necessary. An initial estimate of T_{0D} [T_{0D}
404 = $[(e_S^* - e_A) - s_3 T_S + s_1 T_D] / (s_1 - s_3)$] and M were obtained following Venturini et al. (2008) where
405 s_1 and s_3 were approximated in T_D and T_S , respectively. However, eq. (13) cannot be directly
406 solved because there are two unknowns in one equation. However, since T_{0D} also depends on LE
407 (Mallick et al., 2016, 2018a), an iterative updation of T_{0D} (and M) was carried out by expressing
408 T_{0D} as a function of LE [$T_{0D} = T_D + (\gamma LE / \rho c_p g_{AS1})$] which is described in detail by Mallick et al.
409 (2016, 2018a) and Bhattarai et al. (2018). In the numerical iteration, s_1 was not updated to avoid
410 numerical instability and it was expressed as a function of T_D .

411 **3.1.2 STIC-TI: Coupling modified MV2007-TI and STIC 1.2**

412 The initiation of the coupling between MV2007-TI and STIC1.2 was executed through linking G_i
413 estimates from the modified MV2007-TI with M estimates from STIC1.2. Having the initial



414 estimates of M (through eq. 13), an initial estimation of G_i was made from eq. (2) where S_r in eq.
415 11 was replaced with the initial estimates of M' . Given the initial estimates of G_i (eq. 2) and R_{Ni}
416 (equations in Appendix B), initial estimation of the conductances, LE_i and H_i were obtained. The
417 process was then iterated by updating T_{0D} [$T_{0D} = T_D + (\gamma LE / \rho c_p g_{AS1})$] and M in every time step
418 (as mentioned in Mallick et al., 2016, 2018a), and re-estimating G_i (using eq. 3), net available
419 energy ($R_{Ni} - G_i$), conductances, LE_i and H_i , until stable estimates of LE_i were obtained. The
420 conceptual block diagram and algorithm flow of STIC-TI is shown in Fig. 3a and Fig 3b,
421 respectively.

422

423

424

425

426

427

428

429

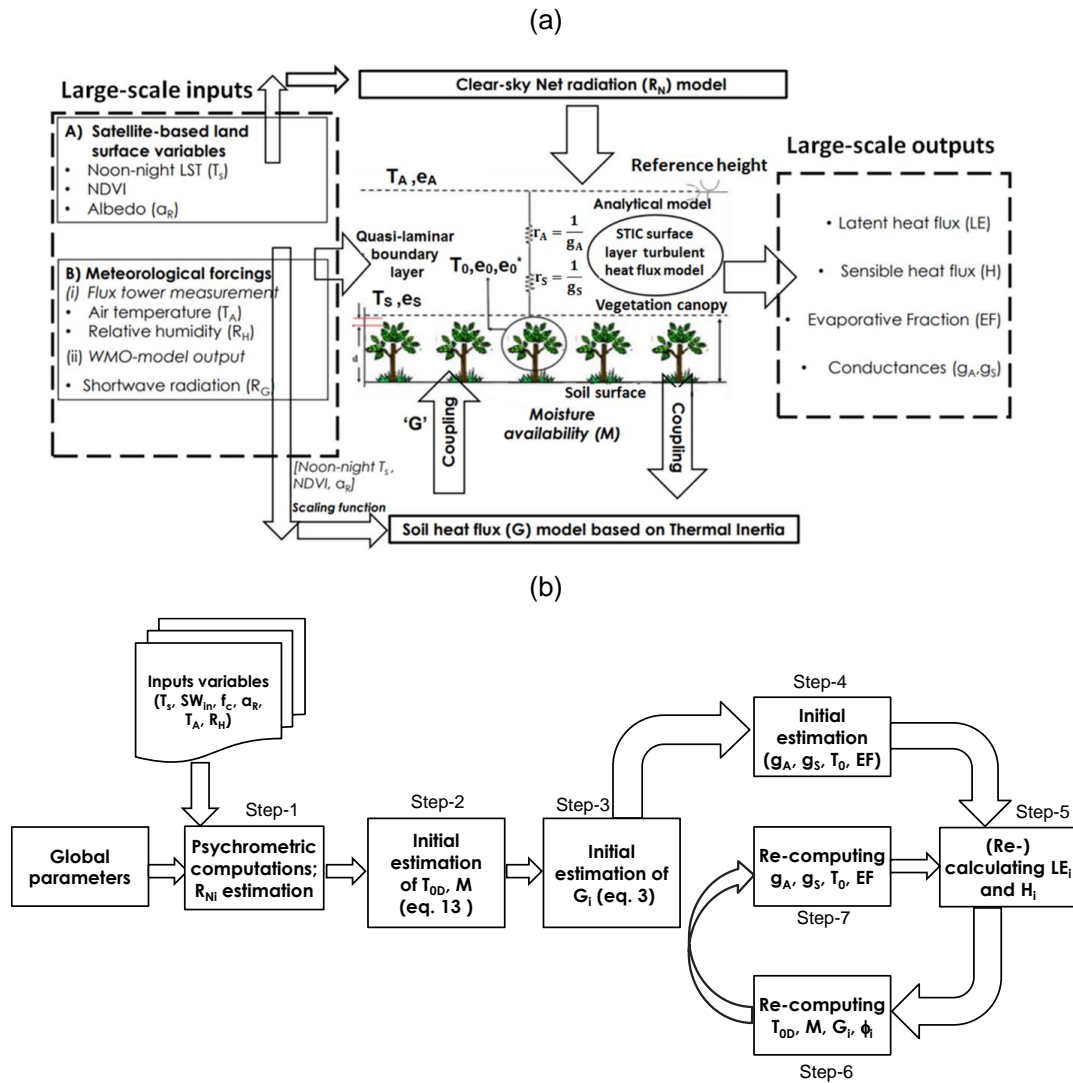


Figure 3: (a) Conceptual diagram of STIC-TI model showing different input variables and model outputs; (b) Algorithmic flow for estimating G and associated SEB fluxes through STIC-TI.

430 Examples of iterative stabilization of G_i and LE_i for Indian, Australian and US ecosystems of India
 431 are shown in Fig. 4. The iterative stabilization of G_i and LE_i was obtained between 8-25 iterations
 432 for all sites.

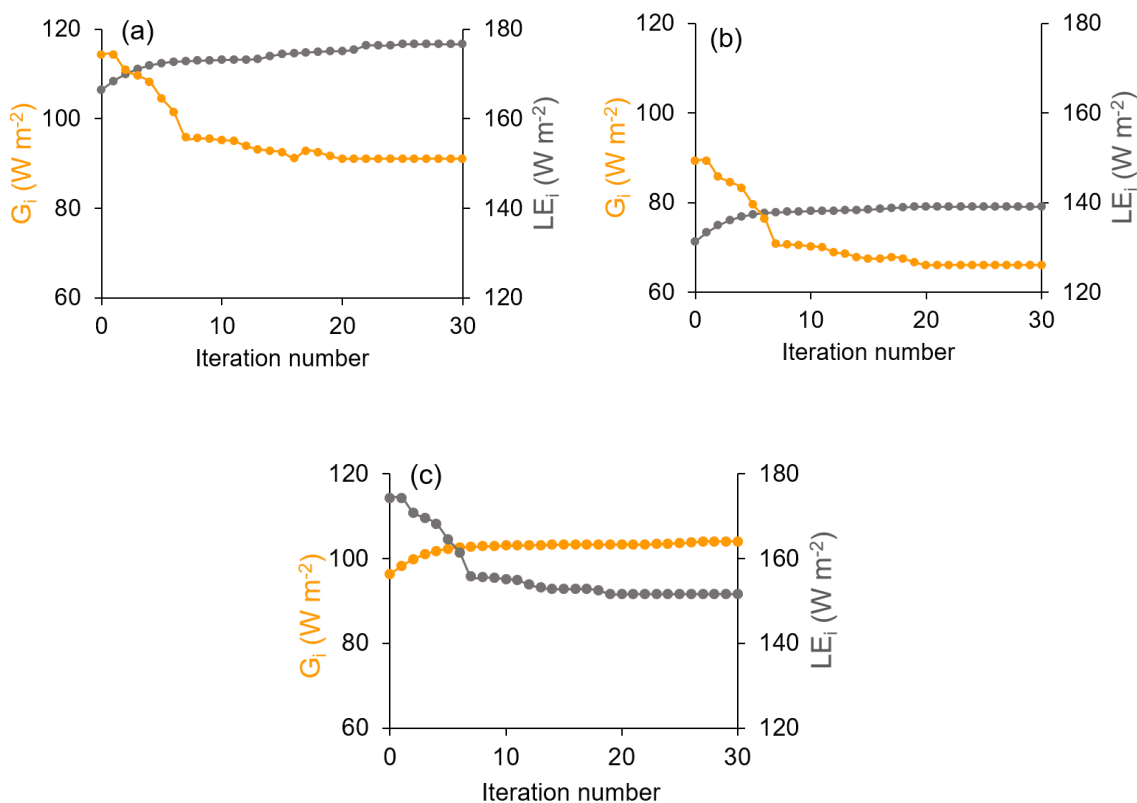


Figure 4: Illustrative examples of iterative stabilization of STIC-TI G_i (yellow marker line) and LE_i (grey marker line) in (a) IND-Jai, (b) AU-ASM, (c) US-Ton

433 3.2 Sensitivity and statistical analysis

434 The accuracy of STIC-TI heavily depends on the accuracy of T_s , NDVI, and α_R due to the dual
435 role of T_s in estimating M and G_i , the role of NDVI in G_i , and the combined role of T_s and α_R in
436 estimating R_{Ni} . Therefore, one-dimensional sensitivity analysis was conducted to assess the
437 impacts of uncertainty in T_s , NDVI and α_R on G_i , H_i and LE_i . The sensitivity was assessed by
438 varying noon-time T_s by ± 0.5 K, ± 1.5 K and ± 1.5 K (keeping nighttime T_s constant so that
439 amplitude can vary automatically); varying NDVI by ± 0.05 ; ± 0.10 , ± 0.15 ; and varying albedo by
440 ± 0.02 , ± 0.05 , ± 0.10 , respectively. SEB fluxes were computed by using T_s , NDVI, and α_R for three
441 different periods of the year in all the eight ecosystems. Sensitivity analyses were conducted by
442 increasing and decreasing systematically T_s , NDVI, α_R from its central value while keeping the
443 other variables and parameters constant. This procedure was selected because the fluxes and



444 intermediate outputs of the STIC-TI model reflect an integrated effect due to uncertainty in T_s . In
 445 the first run, SEB fluxes were computed using *in-situ* T_s measurements obtained from the flux
 446 tower outgoing longwave radiation measurements. Then T_s was increased and decreased at
 447 constant interval and a new set of fluxes were estimated. In the similar way, α_R and NDVI were
 448 increased and decreased at constant intervals and new set of fluxes were computed. The sensitivity
 449 of STIC-TI was assessed by the equation 14.

$$\text{Sensitivity} = \frac{E_{i0} - E_{iM}}{O_i} * 100 \quad (14)$$

450 E_{i0} is the estimated (original) model output and E_{iM} is the estimated (modified) output obtained by
 451 changing the variable whose sensitivity is to be tested. O_i is actual measurements. Apart from the
 452 sensitivity analysis, the following set of statistical metrics were used to assess model performances.

$$R^2 = \left(\frac{\sum_{i=1}^n (E_i - \bar{E})(O_i - \bar{O})}{\sqrt{\sum_{i=1}^n (E_i - \bar{E})^2} \sqrt{\sum_{i=1}^n (O_i - \bar{O})^2}} \right)^2 \quad (15)$$

$$\text{RMSE} = \sqrt{\sum_{i=1}^n \frac{(E_i - O_i)^2}{n}} \quad (16)$$

$$\text{BIAS} = \frac{\sum_{i=1}^n (E_i - O_i)}{n} \quad (17)$$

$$\text{MAPD} = \frac{100}{n} \sum_{i=1}^n \left| \frac{E_i - O_i}{O_i} \right| \quad (18)$$

$$\text{KGE} = 1 - \sqrt{(r - 1)^2 + \left(\frac{\sigma_E}{\sigma_O} - 1 \right)^2 + \left(\frac{\bar{E}}{\bar{O}} - 1 \right)^2} \quad (19)$$

453 Where R^2 is the coefficient of determination, RMSE is root-mean-square error, BIAS is the mean
 454 bias, MAPD is the mean absolute percent deviation, KGE is Kling-Gupta efficiency, n is the total
 455 number of data pairs, the bar indicates mean value of the measured variable and model estimates
 456 of the same variable. E_i and O_i are the model estimated and measured SEB fluxes, r is the Pearson's
 457 correlation coefficient and \bar{O} is the average of measured values and \bar{E} is the average of estimated



458 values and σ_o is standard deviation of observation values and σ_E is the standard deviation of
459 estimated values. The KGE has been widely used for calibration and evaluation hydrological
460 models in recent years and it combines the three components of Nash-Sutcliffe efficiency (NSE)
461 of model errors (i.e. correlation, bias, ratio of variances or coefficients of variation) in a more
462 balanced way. But it has not been widely used for analyzing the ET model performances. $KGE = 1$
463 indicates perfect agreement between modelled estimates and observations. The performance of a
464 model is considered ‘poor’ for KGE between 0 and 0.5 and models with negative KGE values is
465 considered ‘not satisfactory’.

466 **4 Results**

467 **4.1 Ecosystem- scale surface soil temperature amplitude (A)**

468 The scaling functions developed to estimate ecosystem-scale (1 km) surface soil temperature
469 amplitude (A) from point-scale T_{STA} were used to estimate G_i . However, before the development
470 of the scaling functions, analysis was carried out to investigate the relationship of soil temperature
471 amplitude between the two different spatial scales. The scatterplot (Fig. 5a) of noon-night LST
472 difference (ΔT_s) versus T_{STA} for different albedo classes showed a linear increase in ΔT_s with
473 increasing T_{STA} . However, some divergence of data points within the cluster were also noticed
474 which could be associated with different albedo (α_R) levels. Bivariate linear function was fitted
475 between T_{STA} as predictand (Y) versus ΔT_s ($T_{sd} - T_{sn}$) and α_R as predictors (X1 and X2,
476 respectively). The function was found to be $Y = 0.59X1 - 51.3X2 + 8.66$ by combining the data
477 of nine ecosystems ($r = 0.86$). The coefficients in the above expressions correspond to B1 (0.59),
478 B2 (51.3), B3 (8.66) of eq. 5 in section 3.1.1.1. The estimated amplitude from this ecosystem-scale
479 predictors and scaling functions was treated as ecosystem-scale surface soil temperature amplitude
480 (A).

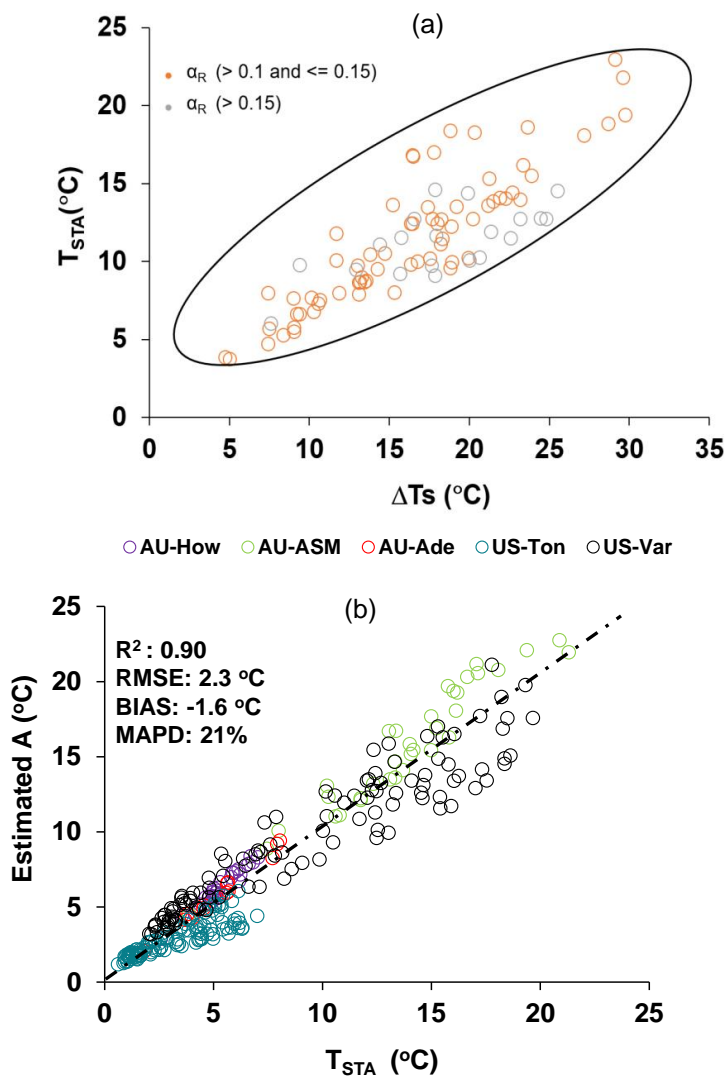


Figure 5. (a) Two-dimensional scatterplots between (ΔTs) versus T_{STA} at different α_R levels over different ecosystems. Here T_{STA} in y-axis is the observed soil temperature amplitude that is used to develop the scaling function and delta ΔTs is noon-night LST difference of MODIS AQUA; (b) Validation of the ecosystem-scale estimates of A from the above functions over different ecosystems and for independent years.

481 The validation of the ecosystem-scale estimates of A from the above functions over different
482 ecosystems is shown in Fig. 5b with respect to T_{STA} for the independent datasets. The estimated A



483 was found to have MAPD of 21%, bias of -1.6°C and $R^2 = 0.90$ over different ecosystems. The
484 temporal variation of estimated A and T_{STA} is shown in Fig D1 in Appendix D.

485 **4.2 Sensitivity analysis of STIC-TI G_i , LE_i and H_i to land surface variables**

486 **4.2.1 Sensitivity of G_i to land surface variables**

487 The average sensitivity of G_i to three land surface variables (T_s , NDVI, α_R) by combining the
488 estimates of wet and dry periods is shown in Fig. 6. G_i was found to be substantially sensitive to
489 T_s with error magnitude ranging from 2 – 18% due to T_s uncertainties of $\pm 0.5 - 2.5$ K (Fig. 6a),
490 with greater sensitivity to T_s during the summer season as compared to other seasons. The median
491 sensitivity of G_i due to $\pm 5 - 10\%$ uncertainty in α_R varied from 5 to 12% in all the ecosystems (Fig.
492 6b). The uncertainties in NDVI revealed 2 to 15% error in G_i estimates (Fig. 6c), and no significant
493 difference in the mean sensitivity due to NDVI uncertainties was noted between the ecosystems.
494 The sensitivity of G_i decreased with increasing values of NDVI.

495 **4.2.2 Sensitivity of LE_i and H_i to land surface variables**

496 Both LE_i and H_i were sensitive to T_s to the order of 2 – 29% (LE_i) and 5 – 35% (H_i) for T_s
497 uncertainty of $\pm 0.5 - 2.5$ K from its mean values (Table 3). Interestingly, LE_i was more sensitive
498 to T_s uncertainties as compared to H_i in the rainfed ecosystems. The highest mean sensitivity of
499 LE_i to T_s was found in arid (IND-Jai: 2 – 28%), semi-arid (AU-ASM: 5 – 21%), tropical savanna
500 (IND-Dha: 3 – 26%), savanna (US-Ton: 4-29%) and arid (US-Var: 3-26%) ecosystems. The mean
501 sensitivity of H_i to T_s was maximum in sub-humid (IND-Sam: 2 – 32%), semi-arid (IND-Naw: 2
502 – 28%), savanna (AU-Ade: 8 – 17%) (Table 3). A greater sensitivity of the SEB fluxes due to α_R
503 uncertainties was found than due to NDVI. The median sensitivity of LE_i and H_i due to 10%
504 uncertainty from mean α_R varied within 2 – 16% in all the ecosystems (Table 3). By contrast,
505 errors in the two SEB fluxes were substantially low (2 – 13%) due to $\pm 0.05 - 0.15$ uncertainty
506 from mean NDVI (Table 3).

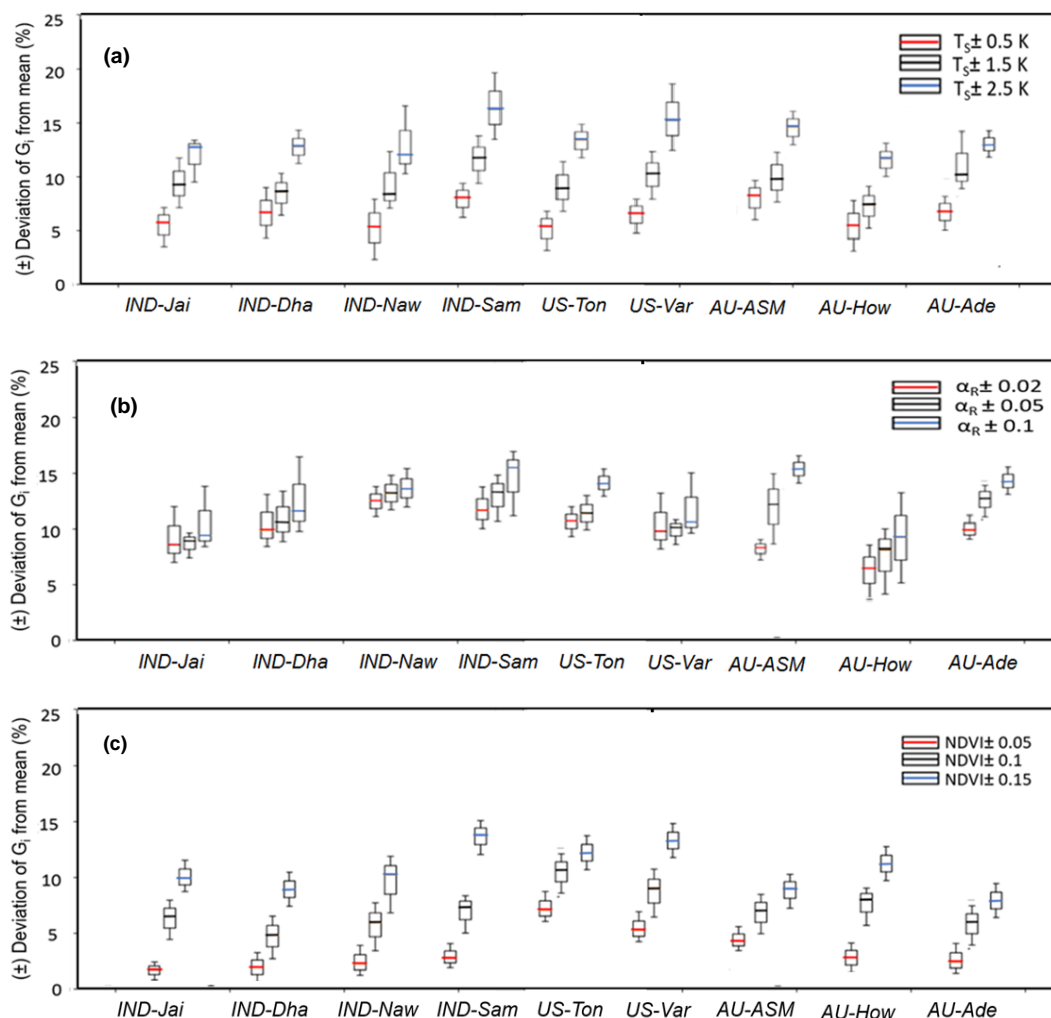


Figure 6: Sensitivity of STIC-TI G_i due to uncertainties in T_s (a), α_R (b), and NDVI (c) for eight flux tower sites in India and Australia. The uncertainties were introduced by taking the mean values of these variables during three different periods (summer, rainy and winter) of a year. Mean uncertainties of the three periods are presented in the figure.



507 **Table 3:** Sensitivity (in percent) of LE_i and H_i due to T_s , NDVI, and α_R uncertainties

Study Sites	Sensitivity of LE_i and H_i to T_s , NDVI and α_R (% range)					
	T_s uncertainty ($\pm 0.5 - 2.5 K$)		α_R uncertainty ($\pm 5 - 10\%$)		NDVI uncertainty ($\pm 0.05 - 0.15$)	
	LE_i	H_i	LE_i	H_i	LE_i	H_i
IND-Jai	2-28	1-6	3-14	2-13	2-8	2-6
IND-Dha	3-26	2-8	2-12	3-12	3-10	3-9
IND-Naw	1-20	2-28	2-10	3-10	2-7	2-6
IND-Sam	1-16	5-32	4-13	6-11	2-5	2-7
US-Ton	4-29	4-12	3-12	4-12	3-8	5-7
US-Var	3-26	6-14	4-11	2-10	4-10	2-8
AU-ASM	5-21	2-10	3-12	2-13	2-10	2-11
AU-How	8-13	2-15	2-11	4-16	3-12	3-13
AU-Ade	2-17	8-17	3-12	2-10	3-10	3-9

508

509 4.3 Comparative evaluation of STIC-TI and contemporary G_i models

510 The performances of STIC-TI and existing G_i models were evaluated and compared with respect
 511 to *in-situ* G_i measurements. The existing models reported by Moran et al. (1989), Bastiaanssen et
 512 al. (1998), Su (2002), and Boegh et al. (2004) have been considered for comparing with TI-based
 513 model. These four existing models are referred here as MOR89, BAS98, SU02 and BO04,
 514 respectively. While the models MOR89, SU02 and BO04 are based on linear regression between
 515 G versus NDVI, BAS98 is based on multivariate regression of G with NDVI, LST and α_R . The
 516 performance of the STIC-TI was substantially better as compared to MOR89, SU02 and BO04
 517 with respect to MAPD (19%), RMSE (22 Wm^{-2}) and coefficient of determination ($R^2 = 0.8$) when
 518 compared with *in-situ* measurements over one Indian, three Australian and two US flux tower sites
 519 (Table 4) and also comparable with BAS98 G_i model. The validation plot of retrieved noontime
 520 G_i from STIC-TI is shown in Fig. 7.

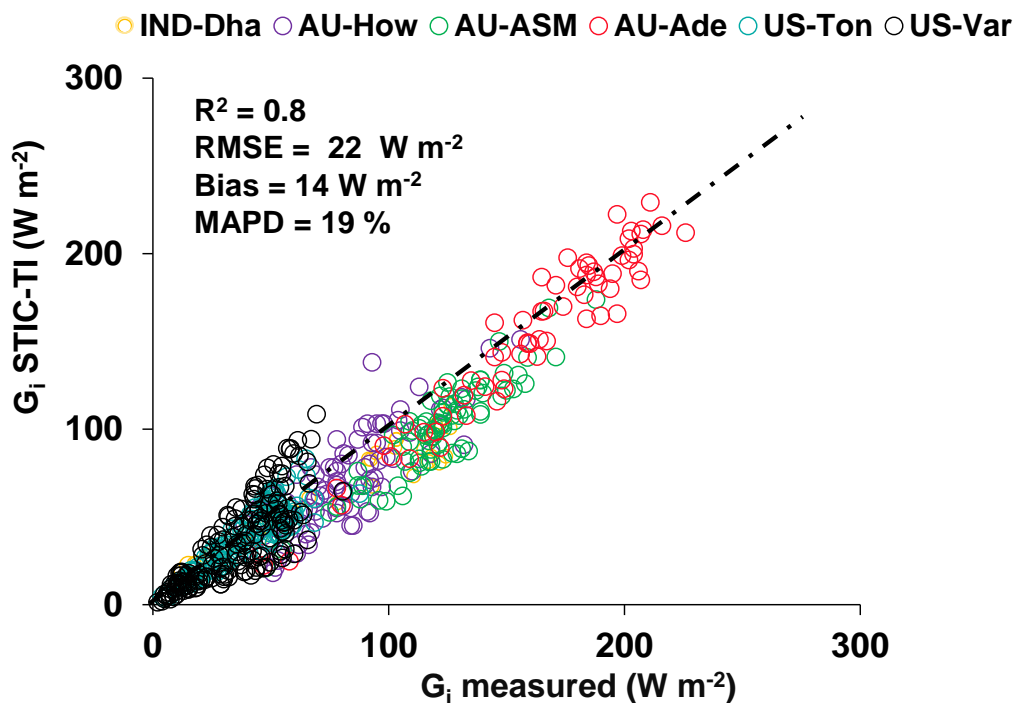


Figure 7: Validation of STIC-TI derived G_i estimates with respect to *in-situ* measurements in different ecosystems. The regression between the two sources of G_i is G_i (STIC-TI) = $0.90G_i$ (tower) - 0.10 .

521 **Table 4:** A comparison of error statistics of G_i estimates from STIC-TI and existing G_i models
 522 over different ecosystems

G models	R ²	RMSE (W m ⁻²)	MAPD (%)	KGE
STIC-TI	0.80	22	19	0.74
MOR89	0.70	31	29	0.46
BAS98	0.80	20	18	0.61
SU02	0.80	30	26	0.54
BO04	0.70	35	29	0.48

523 The RMSE varied from 9 to 20 W m⁻² with MAPD ranging from 12 to 21% across individual flux
 524 tower sites. High magnitude of G_i was predicted in the arid and semi-arid systems (120 – 240 W
 525 m⁻²) as compared to the humid systems (20 – 90 W m⁻²), which was in close correspondence with
 526 the observations. The model also captured the range of G_i that are generally found in different
 527 biomes (20 – 140 W m⁻² for grasslands, 20 – 90 W m⁻² for cropland) (Purdy et al., 2016). Due to



528 the paucity of G_i measurements, direct validation of G_i was only possible for 32 days (concurrent
 529 to MODIS overpass) at the IND-Dha site. Overall, STIC-TI tends to provide reasonable G
 530 estimates for the terrestrial ecosystems having soil temperature amplitude above 5°C .

531 4.4 Evaluation of STIC-TI LE_i , H_i , and EF

532 The modelled versus measured LE_i and H_i showed good agreement in all the nine ecosystems with
 533 RMSE in LE_i and H_i estimates to the order of $29 - 62 \text{ W m}^{-2}$ and $26 - 61 \text{ W m}^{-2}$, MAPD of $9 -$
 534 31% and $20 - 36\%$, BIAS of -29 to 38 W m^{-2} and -44 to 32 W m^{-2} (Fig. 8a, b; Table 5) and high
 535 R^2 of 0.8.

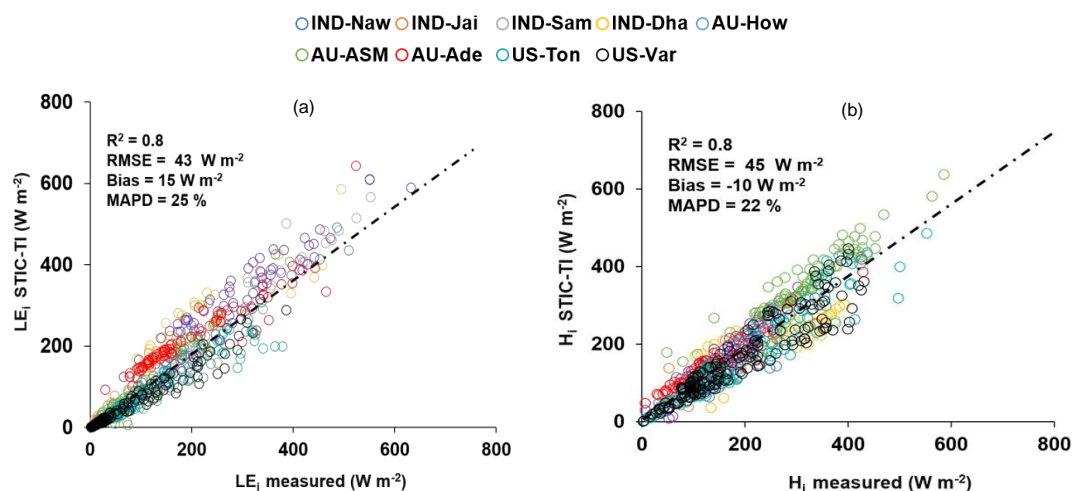


Figure 8: (a) Validation of STIC-TI LE_i estimates with respect to *in-situ* measurements in different ecosystems.; (b) Validation of STIC-TI H_i estimates with respect to *in-situ* measurements in different ecosystems.

536

537 **Table 5:** Error statistics of STIC-TI LE_i and H_i estimates with respect to EC measurements in different
 538 ecosystems of India, US, and Australia.

Sites	STIC- TI (LE_i and H_i)				
	R^2	BIAS (W m^{-2})	RMSE (W m^{-2})	MAPD (%)	KGE



	LE _i	H _i	LE _i	H _i	LE _i	H _i	LE _i	H _i	LE _i	H _i
IND-Jai	0.87	0.85	-21	12	57	27	31	22	0.80	0.76
IND-Naw	0.89	0.85	19	-26	44	51	17	28	0.92	0.71
IND-Dha	0.92	0.91	38	-44	43	35	27	25	0.71	0.64
IND-Sam	0.85	0.81	12	-10	32	61	9	27	0.95	0.70
US-Ton	0.86	0.88	-29	-32	53	34	25	17	0.85	0.91
US-Var	0.84	0.79	-19	-28	49	39	27	20	0.82	0.89
AU-ASM	0.91	0.89	-3	22	46	26	29	20	0.94	0.83
AU-How	0.88	0.86	16	-25	42	27	17	21	0.89	0.85
AU-Ade	0.86	0.85	21	15	29	53	28	36	0.77	0.80

539 Arid ecosystems in India (IND-Jai), US (Ton and Var) and semi-arid ecosystem in Australia (AU-
 540 ASM) revealed relatively high MAPD (31%, 25%, 27%, and 28%) (Table 5). In general, STIC-TI
 541 was able to produce the dominant convective heat fluxes with respect to the EC measurements as
 542 evident through low RMSE for H_i and high RMSE for LE_i in the IND-Jai, US-Ton, US-Var, and
 543 AU-Ade where LE_i is inherently low except few rainy days. A uniform distribution of data points
 544 around 1:1 validation line (Fig. 8a) indicated overall low BIAS in LE_i estimates. However,
 545 modeled H_i was consistently lower than the observations (negative BIAS) in the tropical savanna
 546 (IND-Dha and AU-How) and semi-arid (IND-Naw) ecosystems [(-44) – (-25) W m⁻² and -26 W
 547 m⁻²] while a consistent positive BIAS was observed in the AU-ASM (semi-arid) and AU-Ade
 548 (savanna), US-Var (arid) (Fig. 8b; Table 5). This consequently led to overall low negative BIAS
 549 (-10 W m⁻²), relatively low R² in H_i (R² = 0.8) as compared to the errors in LE_i (BIAS = 15 W m⁻²,
 550 R² = 0.9). The regression between the modeled and tower measurements of LE_i is LE_i(STIC-TI)



551 = $0.98LE_i(\text{tower}) - 0.266$. The regression between the modeled and tower measurements of H_i is
 552 $H_i(\text{STIC-TI}) = 0.93H_i(\text{tower}) + 4.90$. The KGE statistics varied in the range of 0.71 – 0.95 for LE_i
 553 and in the range of 0.64 – 0.91 for H_i , respectively across all nine flux tower sites, thus revealed
 554 reasonably high efficiency of the model to capture the magnitude and variability of SEB fluxes.

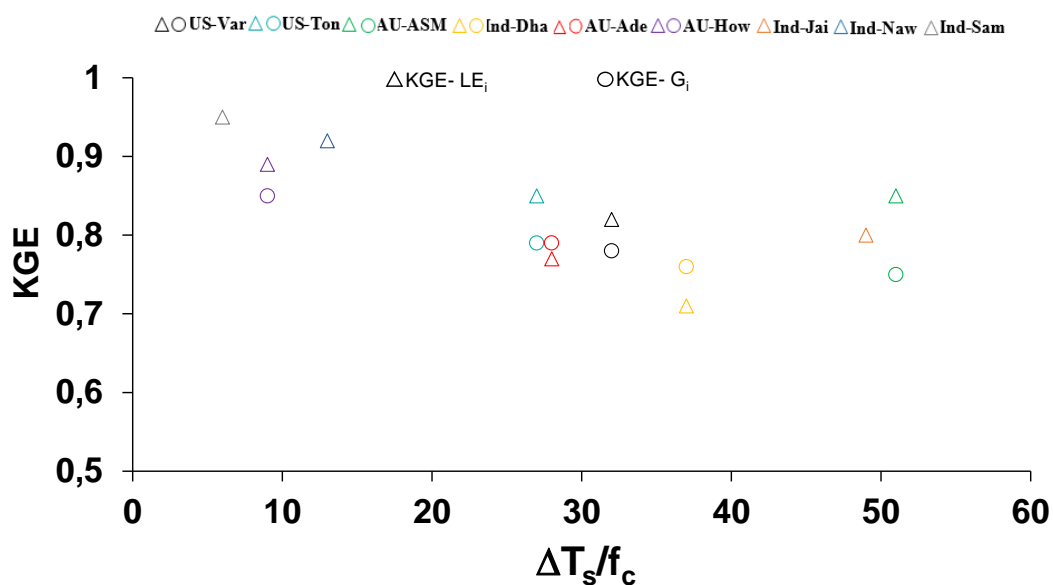


Figure 9: Relationship between KGE of STIC-TI (G_i and LE_i) with $\Delta T_s/f_c$ in different terrestrial ecosystems.

555 Further investigation was made on whether KGE for STIC-TI G_i and LE_i follow any systematic
 556 pattern and the ratio ΔT_s and f_c was used as proxy for surface heterogeneity and dryness. The plot
 557 of KGE of G_i and LE_i with this ratio is shown in Fig. 9. KGE- G_i was found to show a systematic
 558 decrease with increase in ΔT_s - f_c ratio up to 40, after which it remained unchanged with increase
 559 in the ratio. Although KGE of LE_i also decreased (20% reduction) with increase in ΔT_s - f_c ratio,
 560 KGE- LE_i was found to increase beyond ΔT_s - f_c 40. This revealed that the model efficiency
 561 remained high (>0.8) within certain dryness limits (ΔT_s - f_c ratio <20 and >50) and the efficiency
 562 reduced moderately (within 0.7 – 0.8) for intermediate dryness.

563 An independent evaluation of multi-temporal heat fluxes over two US flux sites for the years 2016-
 564 2018 is shown in Fig. 10. STIC-TI G_i estimates showed close match with *in-situ* measurements
 565 with respect to intra and inter-annual variability in G_i followed by LE_i and H_i . This further



566 demonstrates the merit of the coupled model for reproducing ecosystem-scale G_i estimates
567 especially for shorter and open canopies.

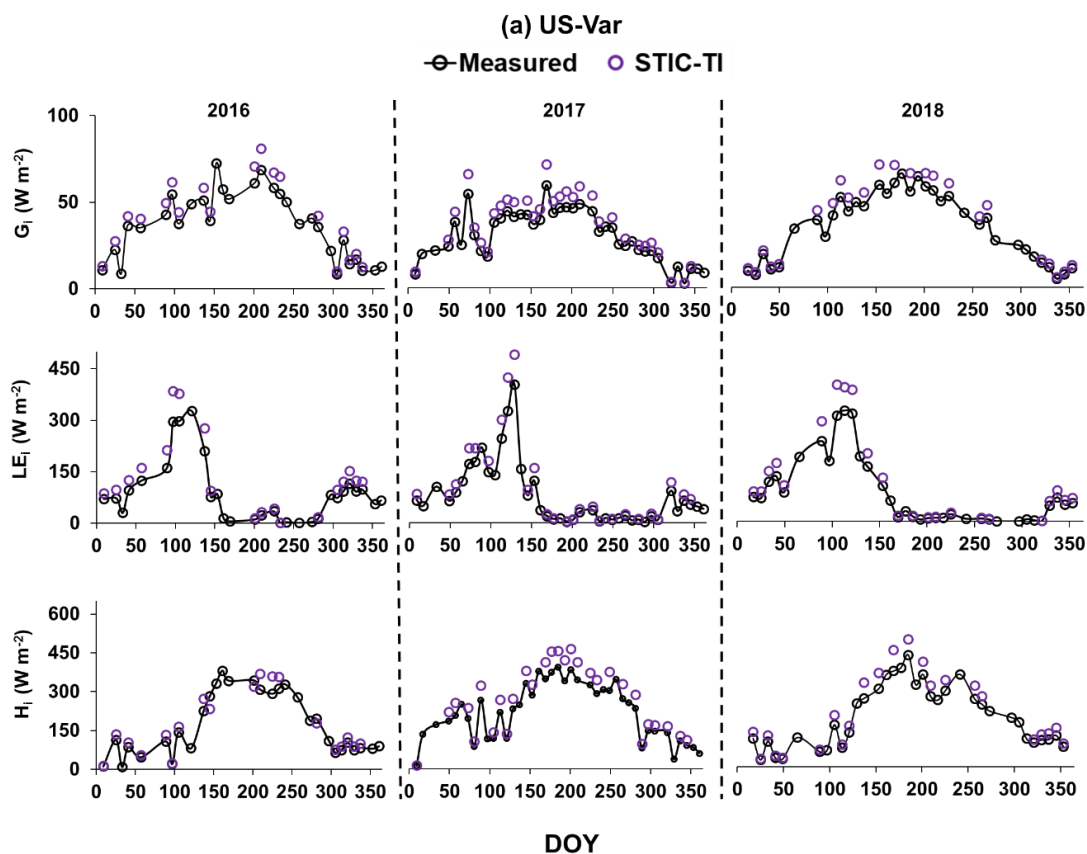


Figure 10 (a): Illustrative examples of temporal evolution of the STIC-TI derived versus observed SEB fluxes for three consecutive years from 2016 to 2018 in a grassland ecosystem in United States (e.g., US-Var).

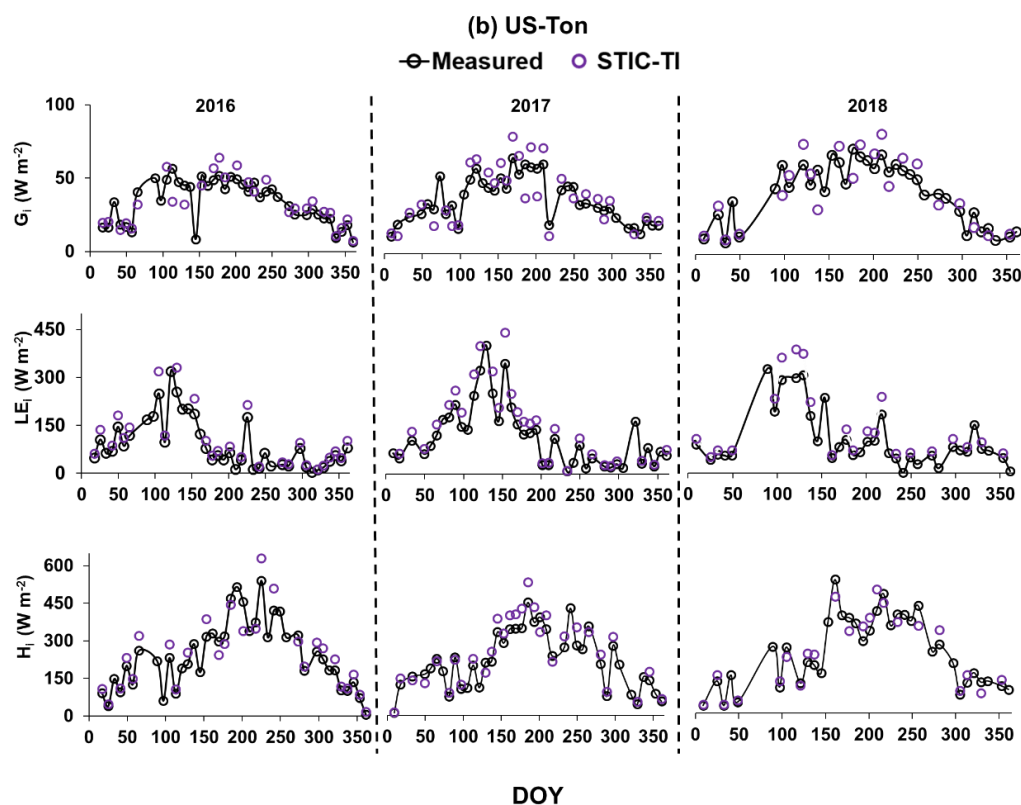


Figure 10 (b): Illustrative examples of temporal evolution of the STIC-TI derived versus observed SEB fluxes for three consecutive years from 2016 to 2018 in a woody savanna ecosystem in the United States (e.g., US-Ton).

568 Temporal behavior of STIC-TI and observed evaporative fraction (EF) (ratio of LE and $R_N - G$)
569 (Fig. 11a) along with observed monthly rainfall (P) distinctly captured the substantial temporal
570 variability in EF during the dry-to-wet transition in the Indian study sites, which also corresponded
571 to low (high) θ and P. In IND-Naw and IND-Sam, a marked rise (>0.4) in STIC-TI EF was noted
572 during day-of-the-year (DOY) 25 to 75 where wheat is grown under assured irrigation. The impact
573 of irrigation is thus captured by the substantial increase in EF in the absence of P. In contrast, the
574 rainfed grassland system (IND-Jai) showed peak EF (~ 0.8), which corresponded to south-west
575 monsoon rainfall during June to September and a progressive decline in EF during the dry down
576 period in October to April corresponding to post south-west monsoon phase. Some intermittent
577 spikes in EF was also noted during dry-down phase in both STIC-TI and observations. This could
578 be due to extra latent heat energy transported through micro-advection from surrounding irrigated



579 agricultural land through the ‘clothesline effect’ which frequently occurs in semi-arid and arid
580 ecosystems. In addition to IND-Jai, the response of both modelled and measured EF to wet and
581 dry spells was also noted during south-west monsoon period at all other flux tower sites of India.

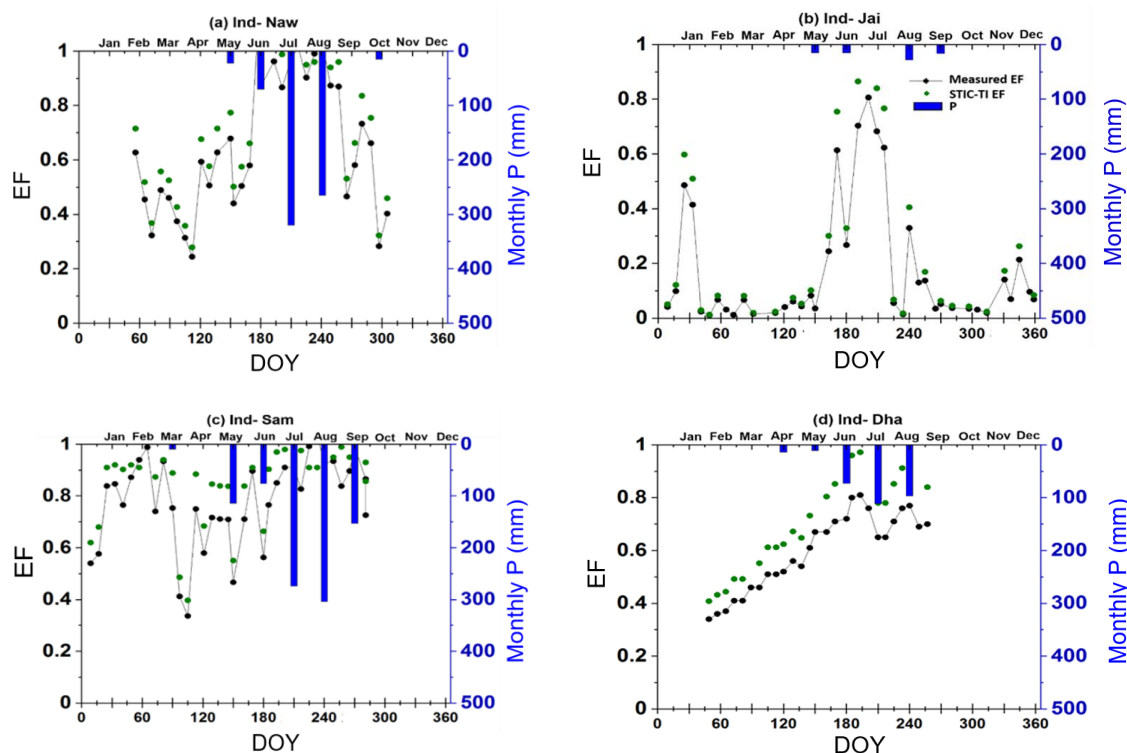


Figure 11a: Illustrative examples of temporal variation of STIC-TI derived EF with respect to measured EF and P in (a) IND-Naw, (b) IND-Jai, (c) IND-Sam, and (d) IND-Dha

582 The temporal behavior of EF from STIC-TI and EC measurements along with measured θ and P
583 at the two OzFlux and AmeriFlux sites also revealed (Fig. 11b) close correspondence of STIC-TI
584 with EC observations. Low EF (0.05 – 0.40) during the dry season around DOY 100 – 250 and
585 high EF (>0.4) during the wet season (DOY 1 – 120 and 300 to 360) in AU-ASM, US-Ton and
586 US-Var was observed. The analysis showed that STIC-TI EF can capture the annual variability of
587 observed EF and its responses across different ecosystems during wet and dry seasons. The plots
588 of STIC-TI EF versus measured θ (in the inset of Fig. 11b) revealed triangular scatter close to
589 right-angled triangle with positive slope of hypotenuse in three ecosystems AU-ASM, US-Var and
590 US-Ton. This showed that in the water-controlled ecosystems, where distinct wet-dry seasons



591 exist, the positive EF- θ relationship is an outcome of the soil moisture controls on transpiration
 592 during the dry season.

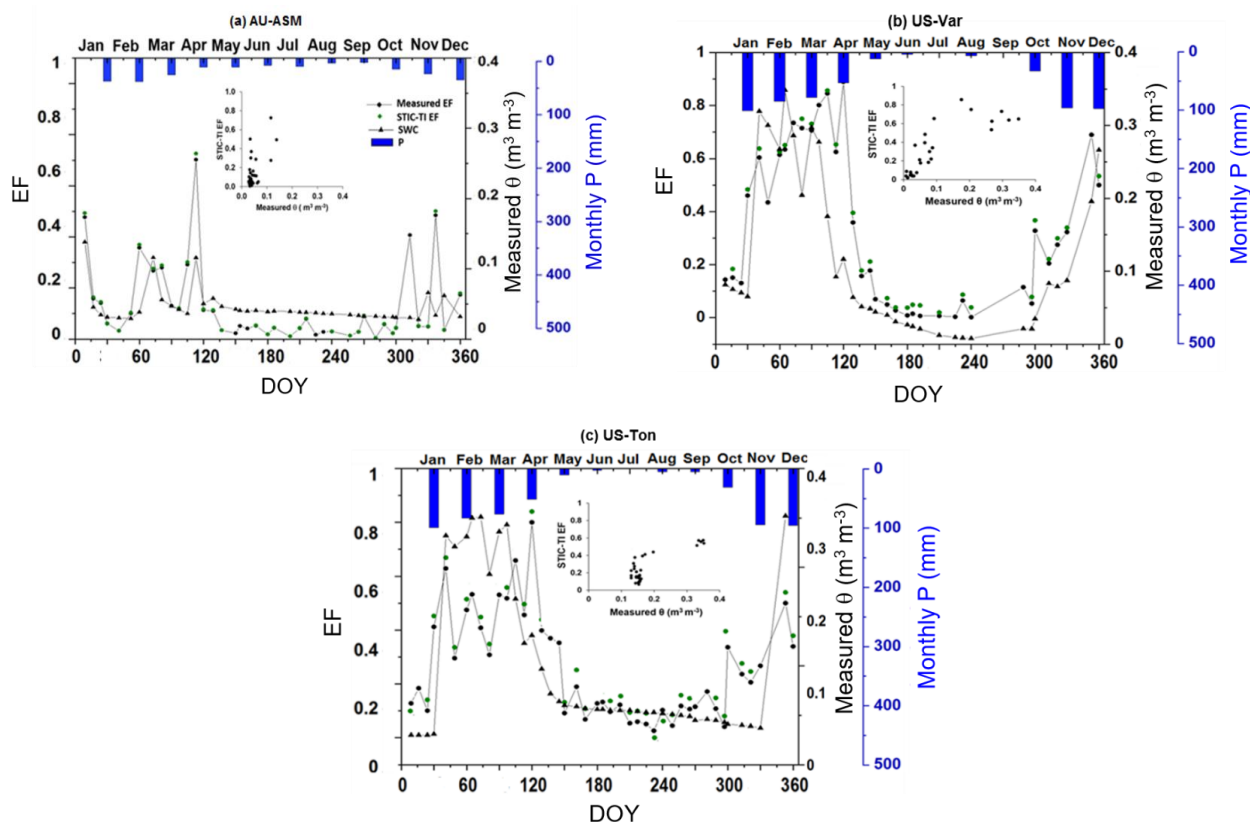


Figure 11b: Comparison of temporal variation of STIC-TI derived EF with respect to measured EF, θ and P in (a) AU-ASM, (b) US-Var, (c) US-Ton. The scatterplots in the inset shows the relationship between STIC-TI EF with respect to measured θ .

593 5 Discussion

594 5.1 Interaction of flux and internal SEB metrics

595 From the section 4.1 we found relatively reduced sensitivity of G_i to T_s uncertainties. In any given
 596 condition, if an over(under) estimation of M due to noontime T_s uncertainties (through eq. 13)
 597 leads to an over(under) estimation of Γ , the effects of such over(under) estimation of Γ (due to
 598 noontime T_s uncertainties) tend to be compensated by the under(over) estimation of amplitude A
 599 (in eq. 5) (Fig. 12d), ultimately leading to a reduction of the sensitivity of G_i to T_s . While the



600 scatter between Γ -M and Γ - T_s (Fig. 12a, b) revealed the sensitivity of G_i to T_s in arid (IND-Jai)
601 and tropical savannah (IND-Dha); which were due to the strong relationship between Γ and
602 daytime T_s (Fig. 12b); the scatter between G_i , Γ , and A (Fig. 12c, d) revealed that the sensitivity
603 of G_i to T_s in semi-arid (IND-Naw) and sub-humid (IND-Sam) ecosystems were due to the strong
604 association between G_i and A.

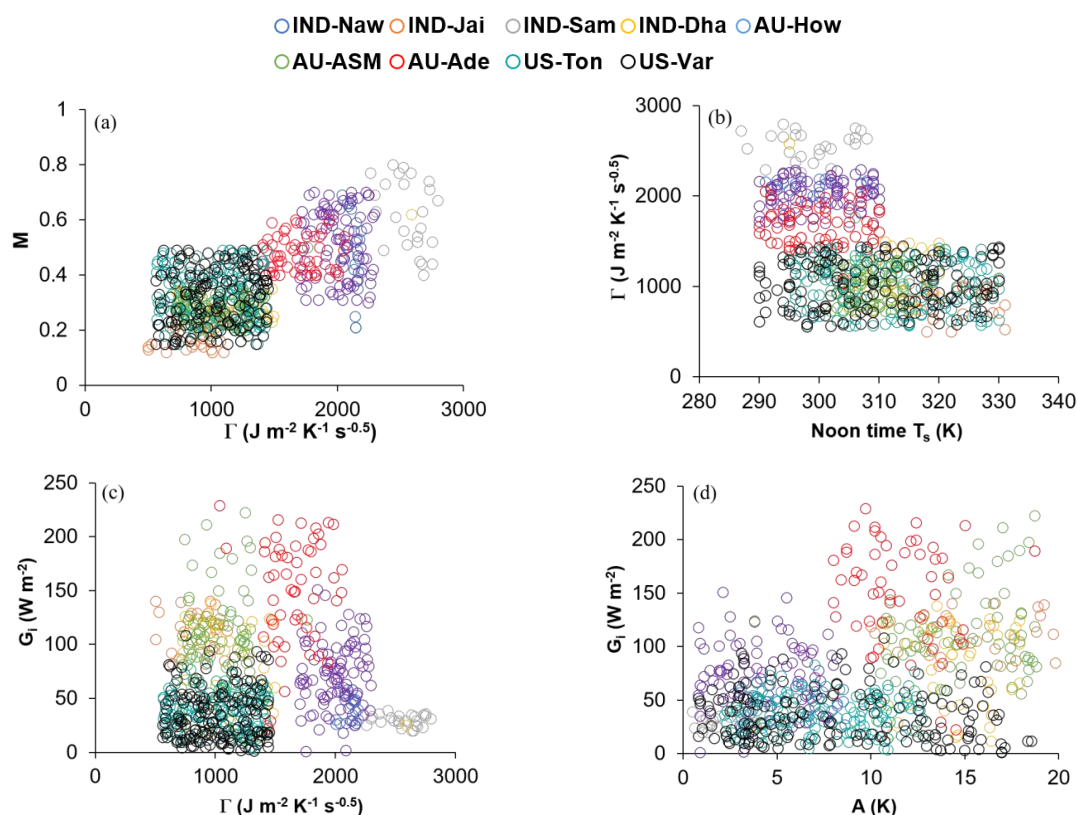


Figure 12: Response plots among parameters of TI-based G_i model, such as (a) Γ vs. M, (b) Γ vs. noon-time T_s , (c) G_i vs. Γ , and (d) G_i vs. A over different ecosystems.

605 Concerning LE_i and H_i , dual uncertainties could be propagated in both the fluxes through
606 daytime T_s (through M and G_i), leading to high sensitivity of these two SEB fluxes due to T_s
607 perturbations. The relatively high sensitivity of LE_i to T_s (as compared to H_i) in the non-
608 irrigated ecosystems could be due to partial compensation of g_A/g_S in both numerator and
609 denominator of the PMEB equation for H (eq. C7 of Appendix C). A recent study (Fig.10 in
610 Mallick et al., 2018a) showed high sensitivity of g_s due to T_s (1% change in T_s led to 5.2–7.5%



611 change in g_s) as compared to g_A sensitivity to T_S (1% change in T_S led to 1.6–2% change in g_A),
612 suggesting that errors in g_s due to T_S uncertainty tend to be larger than errors in g_A . Partial
613 cancellation of the conductance errors in the numerator of eq. (C7 of Appendix C) might have
614 resulted in compensation of H_i errors in the water-limited ecosystems. In this environment, the
615 variability of LE_i is mainly dominated by g_A/g_s , which makes LE_i highly sensitive due to T_S
616 uncertainties. Combined uncertainty due to g_A/g_s in the denominator and g_A in the numerator
617 of eq. (C6 of Appendix C) resulted into greater sensitivity in LE_i to T_S in the arid and tropical
618 savannah ecosystems (Mallick et al., 2015, 2018a; Winter & Eltahir, 2010). The very low
619 sensitivity of LE_i and H_i due to uncertainties in NDVI is because NDVI was not used in the
620 conductance parameterizations and effects due to NDVI in STIC-TI was only propagated
621 through G_i . The sensitivity of LE_i and H_i to albedo was mainly due to the dependence of net
622 radiation (R_{Ni}) on albedo, and any resultant uncertainty in R_{Ni} (due to albedo) tends to be
623 reflected in the sensitivity of LE_i and H_i to albedo.

624 **5.2 Possible sources of errors in SEB flux evaluation**

625 In STIC-TI, underestimation and overestimation errors in G_i in different ecosystems (Fig. 7) could
626 originate due to the errors in MOD11A1 LST product. A host of studies previously reported T_S
627 error of MOD11A1 LST product in the range of 2-3 K with a standard deviation of 0.009, which
628 is mainly due to errors in surface emissivity correction (Duan et al., 2017; Wan, 2014; Lei et al.,
629 2018). In the present analysis, we found an overestimation error of MODIS T_S in the range of 0.5
630 – 1.5 K when compared with *in-situ* infrared temperature measurements at the tropical savanna
631 site. As mentioned in section 3.1, a positive (negative) bias in T_S would tend to an overestimation
632 (underestimation) of amplitude (A) in eq. (5); underestimation (overestimation) of M in eq. (13),
633 and consequent underestimation (overestimation) of Γ (eq. 12) and G_i , respectively. Furthermore,
634 the standard deviation of NDVI surrounding the tower sites varied from 0.01 – 0.05 when
635 compared to the ground measurements, which could be another source of error in the STIC-TI
636 model. In addition, NDVI saturates at $LAI > 3$. However, STIC-TI provides direct estimates of
637 ecosystem G and is independent of R_N . The higher accuracies of TI-based thermal diffusion model
638 as compared to R_N dependent empirical G models were also reported by Purdy et al. (2016) at
639 daily or longer time scales in cropland, grassland. All these G model estimates many a times differ



640 from in situ measurements because of the no accounting of leaf litter presence or layer on soil floor
641 in the remote sensing-based G-model.

642 The overestimation (underestimation) of LE_i (H_i) is also due to the effects of spatial resolution of
643 different input variables on these two SEB fluxes and conducted statistical evaluation with respect
644 to the measured SEB fluxes. Eswar et al. (2017) demonstrated the need for spatial disaggregation
645 models for monitoring LE_i at field scale using contextual models by disaggregation of evaporative
646 fraction (Λ) and downwelling shortwave radiation ratio (R_G). Using different disaggregation
647 models, they estimated LE_i at 250m spatial resolution and reported RMSE of $30 - 32 \text{ W m}^{-2}$ as
648 compared to LE_i obtained at 1000m spatial resolution with RMSE of $40 - 70 \text{ W m}^{-2}$ over different
649 sites in India. Anderson et al. (2007) reviewed different validation experiments conducted in
650 diverse agricultural landscapes (Anderson et al., 2004, 2005; Norman et al., 2003) and reported
651 RMSE in LE_i in the range of $35 - 40 \text{ W m}^{-2}$ (15%) at $30 - 120 \text{ m}$ disaggregated spatial resolution.
652 Current analysis also brought out the need for noon-night thermal imaging with spatial resolution
653 finer than 1000m to adequately capture the magnitude and variability of LE_i in the terrestrial
654 ecosystems especially agroecosystems where average field sizes are less ($< 0.5 \text{ ha}$) and fragmented
655 such as in India and other sub-continent.

656 As seen in Fig. 8a and Table 5, there is a gross overestimation of LE_i with respect to the tower
657 observations. The consistent positive BIAS in STIC-TI LE_i in five out of nine sites is presumably
658 due to the overestimation of R_{Ni} (Figure B1 of Appendix B) and underestimation of G_i . Figure 7
659 shows overestimation of G_i for three OzFlux sites and US sites and underestimation of G_i for Indian
660 site with G_i (STIC-TI) = $0.90 G_i(\text{tower}) - 0.10$ and overestimation of R_{Ni} at the ecosystem-scale,
661 with R_{Ni} (STIC-TI) = $0.78R_{Ni}(\text{tower}) + 58.92$ (Appendix-B2). This means a systematic
662 overestimation of the net available energy ($R_{Ni} - G_i$) will be obvious in cases where STIC-TI shows
663 underestimation of G_i , which consequently leads to an overestimation of retrieved LE_i .

664 **5.3 Effects of SEB closure**

665 Using the unclosed SEB observations for Indian sites in absence of *in-situ* G_i observations also
666 added to the consistent positive BIAS in the statistical evaluation of LE_i . A widespread lack of
667 energy balance closure to the order of 10 – 20% worldwide at most of the EC sites is reported in
668 the literature (Stoy et al., 2013; Wilson et al., 2002), which implies a systematic underestimation
669 (overestimation) of $LE_i(\text{EC tower})$ (and/or $H_i(\text{EC tower})$). Accommodating an average 15%



670 imbalance in LE_i (EC tower) would tend to diminish the positive BIAS in STIC-TI. Therefore, the
671 pooled gain (0.98) and positive BIAS between the STIC-TI and tower LE_i is determined by the
672 overestimation of $(R_{Ni} - G_i)$, combined with the underestimation of measured LE_i from the EC
673 towers. An underestimation of H_i (negative BIAS) is associated with two reasons; (a) ignoring the
674 two-sided aerodynamic conductance of the leaves (Jarvis and McNaughton, 1986; Monteith and
675 Unsworth, 2013; Schymanski et al., 2017), which could lead to substantial underestimation of H_i ,
676 and (b) due to the complementary nature of the PMEB equation, if LE_i is overestimated, H_i will
677 be underestimated. In addition, frequent micro-advection fluxes alter measured in situ H and LE
678 fluxes. But these advection conditions are not explicitly accounted in the current STIC-TI model.

679 **6 Summary and conclusions**

680 This study addressed one of the outstanding challenges in retrieving ground heat flux (G) and
681 evaporation (ET) in open canopy, water-controlled and radiation-controlled ecosystems. It
682 demonstrated coupling of a thermal inertia (TI)-based mechanistic G model with an analytical
683 surface energy balance (SEB) model (Surface Temperature Initiated Closure, STIC) using
684 satellite-based land surface temperature (T_s) and associated biophysical variables and has minimal
685 independence on *in-situ* measurements. The model is called STIC-TI, and this is the first ever
686 implementation of a coupled G-SEB model that does not require any empirical parameterization
687 of aerodynamic and canopy-surface conductance. By linking T_s with thermal inertia (Γ) and
688 surface moisture availability (M), STIC-TI derives G through the harmonics equation between G
689 and Γ , and subsequently coupled G with the SEB fluxes. For estimating Γ , this paper also
690 developed scaling functions for ecosystem-scale surface soil temperature amplitude (A) through
691 bivariate regression between the observed soil temperature versus remote sensing derived T_s and
692 surface albedo. Independent validation of STIC-TI using measured flux data from nine terrestrial
693 ecosystems in arid, semi-arid and sub-humid climate in India, USA (representing northern
694 hemisphere) and Australia (representing southern hemisphere) led us to the following conclusions:

695 (i) The retrieved G_i and associated SEB fluxes through STIC-TI were reasonably sensitive to
696 uncertainties in T_s and vegetation index. However, a compensation effect was evident due to
697 the partial cancellation of overestimated TI and underestimated A in the harmonics equation
698 of G. Both, latent and sensible heat fluxes (LE and H), were extremely sensitive to T_s



699 uncertainties. While the maximum sensitivity of LE to T_S was found in the arid and semi-arid
700 ecosystems, the sensitivity of H to T_S was maximum in the sub-humid ecosystems.

701 (ii) G_i estimates through STIC-TI performed better as compared to most of the contemporary
702 empirical G models. It showed lower mean absolute percent deviation (MAPD) of 19% and
703 higher correlation coefficient (0.8) with respect to *in-situ* measurements for different
704 ecosystems. Despite the error statistics, G from STIC-TI was comparable to the existing semi-
705 empirical G model of Bastiaanssen et al. (1998) (BAS98), this coupled model has certain
706 advantages such as, (a) it provides direct estimates of G and is not dependent on net radiation
707 estimates, (b) the ecosystem-scale surface soil temperature amplitude used in G model can
708 advance our understanding on associated terrestrial ecosystem processes.

709 (iii) Overall, the STIC-TI explained significant variability in the measured SEB fluxes with a
710 MAPD of 19% for instantaneous G and 22 – 25% for instantaneous LE and H. The model
711 efficiency (KGE) was greater than 0.7 for G and LE in all the nine ecosystems having
712 contrasting aridity and canopy cover. Underestimation tendency of G in some ecosystems was
713 primarily attributed to the inherent bias in MODIS T_S product, NDVI saturation at higher LAI
714 (>3) in conjunction with the spatial scale mismatch between single MODIS pixel and the
715 footprint of G measurements. The consequent overestimation (underestimation) of LE (H) in
716 some ecosystems was associated with the overestimation of the net available energy, use of
717 ‘unclosed’ SEB observation in the validation of LE and H, the spatial scale discrepancy
718 between MODIS pixel versus eddy covariance measurement footprint, the complementary
719 nature of the Penman Monteith Energy Balance equation (for H), and possibly due to ignoring
720 the two-sided aerodynamic conductance by the leaves (for H).

721 The requirement of few input variables in STIC-TI generates promise for surface-atmosphere
722 exchange studies using readily available data from the current generation remote sensing satellites
723 (e.g., MODIS, INSAT) that have noon-night TIR observations. Current findings also provide
724 motivation in refining G simulation in the land surface models. STIC-TI can be potentially used
725 for distributed ET mapping using current and future 4th generation Indian Geostationary satellite
726 observations from INSAT as well as future high spatial resolution (~ 60m) TIR observations with
727 3-day revisit from polar orbiting platform (Lagouarde et al., 2018, 2019) through the planned Indo-
728 French space-borne mission, TRISHNA (Thermal infrared Imaging Satellite for High-resolution
729 Natural Resource Assessment). This simple approach will also help in catering the need for a



730 reliable, space-time continuous ET datasets in data-poor regions like Indian sub-tropics, South-
731 East Asia and other parts of the world from thermal remote sensing observation.

732 **Author contributions**

733 KM and BKB conceptualized the idea; DD conducted STIC-TI model coding, simulations and
734 data analysis in consultation with KM and BKB; DD and BKB wrote the first version of the
735 manuscript with KM writing the introduction, discussions and conclusions; all authors contributed
736 to discussions, editing and corrections; BKB and KM jointly finalized the manuscript.

737 **Acknowledgement**

738 The authors gratefully acknowledge Ministry of Earth Sciences (MoES), Govt. of India and
739 National Environmental Research Council for providing necessary support through Indo-UK
740 INCOMPASS programme (NE/L013819/1, NE/L013843/1, NE/L01386X/1, NE/P003117/1).
741 BKB acknowledges Deputy Director, EPSA, SAC-ISRO and Director, SAC-ISRO for providing
742 necessary support to participate and contribute to Indo-UK INCOMPASS programme. DD
743 acknowledges Prof. P.D. Lele and Head from Department of Physics, Electronics and Space
744 Sciences, Gujarat University Ahmedabad and for providing the necessary support to carry out this
745 work. KM was supported by the Luxembourg Institute of Science and Technology (LIST) and
746 through the doctoral training unit and through the Mobility OUT fellowship of Luxembourg
747 National Research Fund (FNR) (PRIDE15/10623093/HYDROCSI;
748 INTER/MOBILITY/2020/14521920/MONASTIC). KCN is supported by the Jet Propulsion
749 Laboratory, California Institute of Technology, under contract with the National Aeronautics and
750 Space Administration and Government sponsorship is acknowledged. DDB acknowledges support
751 from NASA Ecostress project and the US Department of Energy, Office of Science which supports
752 the AmeriFlux project

753 **Data and code availability**

754 Harmonized time series datasets over the study grids are available in
755 <https://doi.org/10.5281/zenodo.5806501>. The model code is available to the first author upon
756 reasonable request.



757 **References**

- 758 Anderson, M., Kustas, W., Alfieri, J., Gao, F., Hain, C., Prueger, J., Evett, S., Colaizzi, P., Howell,
759 T. and Chávez, J.: Mapping daily evapotranspiration at Landsat spatial scales during the
760 BEAREX'08 field campaign, *Adv. Water Resour.*, 50, 162 – 177,
761 <https://doi.org/10.1016/j.advwatres.2012.06.005>, 2012.
- 762 Anderson, M., Norman, J., Kustas, W., Li, F., Prueger, J. and Mecikalski, J.: Effects of Vegetation
763 Clumping on Two-Source Model Estimates of Surface Energy Fluxes from an Agricultural
764 Landscape during SMACEX, *J. Hydrometeorol.*, 6(6), 892 – 909,
765 <https://doi.org/10.1175/JHM465.1>, 2005.
- 766 Anderson, M., Norman, J., Mecikalski, J., Otkin, J. and Kustas, W.: A climatological study of
767 evapotranspiration and moisture stress across the continental United States based on thermal
768 remote sensing: 1. Model formulation, *J. Geophys. Res.: Atmos.*, 112(D10),
769 <https://doi.org/10.1029/2006JD007506>, 2007.
- 770 Anderson, M., Norman, J., Mecikalski, J., Torn, R., Kustas, W. and Basara, J.: A Multiscale
771 Remote Sensing Model for Disaggregating Regional Fluxes to Micrometeorological Scales, *J.*
772 *Hydrometeorol.*, 5(2), 343 – 363, [https://doi.org/10.1175/1525-
773 7541\(2004\)005<0343:AMRSMF>2.0.CO;2](https://doi.org/10.1175/1525-7541(2004)005<0343:AMRSMF>2.0.CO;2), 2004.
- 774 Bai, Y., Zhang, S., Bhattarai, N., Mallick, K., Liu, Q., Tang, L., Im, J., Guo, L., and Zhang, J.: On
775 the use of machine learning based ensemble approaches to improve evapotranspiration
776 estimates from croplands across a wide environmental gradient, *Agric. Forest Meteorol.*, 298
777 - 299, 108308, <https://doi.org/10.1016/j.agrformet.2020.108308>, 2021.
- 778 Zerefos, C. S., & Bais, A. F.: *Solar Ultraviolet Radiation: Modelling, Measurements and*
779 *Effects*, Springer Berlin Heidelberg, 2013.
- 780 Bastiaanssen, W. G. M., Menenti, M., Feddes, R. A. and Holtslag, A. A. M.: A remote sensing
781 surface energy balance algorithm for land (SEBAL). 1. Formulation, *J. Hydrol.*, 198-212,
782 doi:10.1016/S0022-1694(98)00253-4, 1998.
- 783 Bennett, W., Wang, J. and Bras, R.: Estimation of Global Ground Heat Flux, *J. Hydrometeorol.*,
784 9(4), 744 – 759, <https://doi.org/10.1175/2008JHM940.1>, 2008.
- 785 Beringer, J., Hutley, L. B., McHugh, I., Arndt, S. K., Campbell, D., Cleugh, H. A., Cleverly, J.,
786 Resco de Dios, V., Eamus, D., Evans, B., Ewenz, C., Grace, P., Griebel, A., Haverd, V.,
787 Hinko-Najera, N., Huete, A., Isaac, P., Kanniah, K., Leuning, R., Liddell, M. J., Macfarlane,



- 788 C., Meyer, W., Moore, C., Pendall, E., Phillips, A., Phillips, R. L., Prober, S. M., Restrepo-
789 Coupe, N., Rutledge, S., Schroder, I., Silberstein, R., Southall, P., Yee, M. S., Tapper, N. J.,
790 van Gorsel, E., Vote, C., Walker, J., and Wardlaw, T.: An introduction to the Australian and
791 New Zealand flux tower network – OzFlux, *Biogeosciences*, 13, 5895–5916, doi:10.5194/bg-
792 13-5895-2016, 2016.
- 793 Bhandari, A., Kumar, A. & Singh, G.K.: Feature Extraction using Normalized Difference
794 Vegetation Index (NDVI): A Case Study of Jabalpur City, *Proc Technol.*, 6, 612–621,
795 <https://doi.org/10.1016/j.protcy.2012.10.074>, 2012.
- 796 Bhat, G., Morrison, R., Taylor, C., Bhattacharya, B., Paleri, S., Desai, D., Evans, J., Pattnaik, S.,
797 Sekhar, M., Nigam, R., Sattar, A., Angadi, S., Kancha, D., Patidar, A., Tripathi, S., Krishnan,
798 K. and Sisodiya, A.: Spatial and temporal variability in energy and water vapor fluxes
799 observed at seven sites on the Indian subcontinent during 2017, *Q. J. R. Meteorolog. Soc.*, 146
800 (731), <https://doi.org/10.1002/qj.3688>, 2853-2866, 2019.
- 801 Bhattarai, N., Mallick, K., Brunzell, N. A., Sun, G., and Jain, M.: Regional evapotranspiration
802 from an image-based implementation of the Surface Temperature Initiated Closure (STIC1.2)
803 model and its validation across an aridity gradient in the conterminous US, *Hydrol. Earth Syst.*
804 *Sci.*, 22, 2311–2341, <https://doi.org/10.5194/hess-22-2311-2018>, 2018.
- 805 Bhattarai, N., Mallick, K., Stuart, J., Vishwakarma, B., Niraula, R., Sen, S. and Jain, M.: An
806 automated multi-model evapotranspiration mapping framework using remotely sensed and
807 reanalysis data, *Remote Sens. Environ.*, 229, 69 – 92,
808 <https://doi.org/10.1016/j.rse.2019.04.026>, 2019.
- 809 Boegh, E., Soegaard, H., Christensen, J. H., Hasager, C. B., Jensen, N.O. and Nielsen, N. W.:
810 Combining weather prediction and remote sensing data for the calculation of
811 evapotranspiration rates: application to Denmark, *Int. J. Remote Sens.*, 25, 2553 - 2574,
812 <https://doi.org/10.1080/01431160310001647984>, 2004.
- 813 Cammalleri, C. and Vogt, J.: On the Role of Land Surface Temperature as Proxy of Soil Moisture
814 Status for Drought Monitoring in Europe, *Remote Sens.*, 7(12), 16849-16864,
815 <https://doi.org/10.3390/rs71215857>, 2015.
- 816 Cano, D., Monget, J., Albuissou, M., Guillard, H., Regas, N. and Wald, L.: A method for the
817 determination of the global solar radiation from meteorological satellite data. *Solar Energy*,
818 37(1), 840, 31 – 39, [https://doi.org/10.1016/0038-092X\(86\)90104-0](https://doi.org/10.1016/0038-092X(86)90104-0), 1986.



- 819 Castelli, F., Entekhabi, D. and Caporali, E.: Estimation of surface heat flux and an index of soil
820 moisture using adjoint-state surface energy balance, *Water Resour. Res.*, 35(10), 3115 – 3125,
821 <https://doi.org/10.1029/1999WR900140>, 1999.
- 822 Didan, K.: MOD13Q1 MODIS/Terra Vegetation Indices 16-Day L3 Global 250m SIN Grid
823 V006., distributed by NASA EOSDIS Land Processes DAAC,
824 doi:10.5067/MODIS/MOD13Q1.006, 2021-06-06, 2015.
- 825 Donohue, R. J., Hume, I. H., Roderick, M. L., McVicar, T. R., Beringer, J., Hutley, L. B., Arndt,
826 S. K.: Evaluation of the remote-sensing-based DIFFUSE model for estimating photosynthesis
827 of vegetation, *Remote Sens. Environ.*, 155, 349–365, doi:10.1016/j.rse.2014.09.007, 2014.
- 828 Drori, R.; Dan, H.; Sprintsin, M.; Sheffer, E. Precipitation-Sensitive Dynamic Threshold: A New
829 and Simple Method to Detect and Monitor Forest and Woody Vegetation Cover in Sub-Humid
830 to Arid Areas. *Remote Sens.*, 12, 1231, doi:10.3390/rs12081231, 2020.
- 831 Duan, A., Wang, M., Lei, Y. and Cui, Y.: Trends in summer rainfall over China associated with
832 the Tibetan Plateau sensible heat source during 1980–2008, *J. Clim.*, 26, 261–75,
833 <https://doi.org/10.1175/JCLI-D-11-00669.1>, 2013.
- 834 Duan, S., Li, Z., Cheng, J. and Leng, P.: Cross-satellite comparison of operational land surface
835 temperature products derived from MODIS and ASTER data over bare soil surfaces. *ISPRS*
836 *J. Photogramm. Remote Sens.*, 126, 1-10, <https://doi.org/10.1016/j.isprsjprs.2017.02.003>,
837 2017.
- 838 Eswar, R., Sekhar, M., Bhattacharya, B. and Bandyopadhyay, S.: Spatial Disaggregation of Latent
839 Heat Flux Using Contextual Models over India, *Remote Sens.*, 9(9), 949,
840 <https://doi.org/10.3390/rs9090949>, 2017.
- 841 Friedl, M., McIver, D., Hodges, J., Zhang, X., Muchoney, D., Strahler, A., Woodcock, C., Gopal,
842 S., Schneider, A., Cooper, A., Baccini, A., Gao, F. and Schaaf, C.: Global land cover mapping
843 from MODIS: algorithms and early results, *Remote Sens. Environ.*, 83(1-2), 287 – 302,
844 [https://doi.org/10.1016/S0034-4257\(02\)00078-0](https://doi.org/10.1016/S0034-4257(02)00078-0), 2002.
- 845 Gao, Z., Horton, R. and Liu, H. P.: Impact of wave phase difference between soil surface heat
846 flux and soil surface temperature on soil surface energy balance closure, *J. Geophys. Res.*,
847 115, D16112, doi:10.1029/2009JD013278, 2010.



- 848 Isaac, P., Cleverly, J., McHugh, I., van Gorsel, E., Ewenz, C., and Beringer, J.: OzFlux data:
849 network integration from collection to curation, *Biogeosciences*, 14, 2903–2928,
850 doi:10.5194/bg-14-2903-2017, 2017.
- 851 Jarvis, P.G. and McNaughton, K.G.: Stomatal Control of Transpiration – Scaling up from Leaf to
852 Region, *Adv. Ecol. Res.*, 15, 1-49, [https://doi.org/10.1016/S0065-2504\(08\)60119-1](https://doi.org/10.1016/S0065-2504(08)60119-1), 1986.
- 853 Johansen, O.: Thermal conductivity of soils, PhD Thesis, University of Trondheim. Hanover, NH:
854 Cold Regions Research and Engineering Laboratory, US Army Corps of Engineers, CRREL
855 Draft English translation, <https://apps.dtic.mil/sti/pdfs/ADA044002.pdf>, 1975.
- 856 Kiptala, J., Mohamed, Y., Mul, M. and Van der Zaag, P.: Mapping evapotranspiration trends using
857 MODIS and SEBAL model in a data scarce and heterogeneous landscape in Eastern
858 Africa, *Water Resour. Res.*, 49(12), 8495 – 8510, <https://doi.org/10.1002/2013WR014240>,
859 2013.
- 860 Kustas, W. and Anderson, M.: Advances in thermal infrared remote sensing for land surface
861 modeling, *Agric. For. Meteorol.*, 149(12), 2071-2081,
862 <https://doi.org/10.1016/j.agrformet.2009.05.016>, 2009.
- 863 Lagouarde J.-P., Bhattacharya BK, Crébassol P., Gamet P., Babu SS, Boulet G., Briottet X.,
864 Buddhiraju KM, Cherchali S., Dadou I., Dedieu G., Gouhier M., Hagolle O Irvine M., Jacob
865 F., Kumar A., Kumar KK, Laignel B., Mallick K., Murthy CS, Oliosio A., Otle C., Pandya
866 MR, Raju PV, Roujean J.-L., Sekhar M., Shukla MV, Singh SK, Sobrino J., Ramakrishnan
867 R.: The Indian-French Trishna Mission: Earth Observation in the Thermal Infrared with High
868 Spatio-Temporal Resolution, *IGARSS 2018 - 2018 IEEE International Geoscience and
869 Remote Sensing Symposium*, Institute of Electrical and Electronics Engineers (IEEE). USA,
870 4078-4081, doi:10.1109/IGARSS.2018.8518720, 2018.
- 871 Lagouarde, J., Bhattacharya, B., Crébassol, P., Gamet, P., Adlakha, D., Murthy, C., Singh, S.,
872 Mishra, M., Nigam, R., Raju, P., Babu, S., Shukla, M., Pandya, M., Boulet, G., Briottet, X.,
873 Dadou, I., Dedieu, G., Gouhier, M., Hagolle, O., Irvine, M., Jacob, F., Kumar, K., Laignel,
874 B., Maisongrande, P., Mallick, K., Oliosio, A., Otlé, C., Roujean, J., Sobrino, J.,
875 Ramakrishnan, R., Sekhar, M. and Sarkar, S.: Indo-French high-resolution thermal infrared
876 space mission for earth natural resources assessment and monitoring – concept and definition
877 of TRISHNA, *ISPRS - International Archives of the Photogrammetry, Remote Sensing and
878 Spatial Information Sciences*, XLII-3/W6, 403-407, 2019.



- 879 Lu, L., Zhang, T., Wang, T. and Zhou, X.: Evaluation of Collection-6 MODIS Land Surface
880 Temperature Product Using Multi-Year Ground Measurements in an Arid Area of Northwest
881 China, *Remote Sens.*, 10(11), 1852, <https://doi.org/10.3390/rs10111852>, 2018.
- 882 Mallick, K., & Bhattacharya, B.K., Chaurasia, S., Dutta, S., Nigam, R., Mukherjee J., Banerjee,
883 S., Kar, G., Rao, V., Gadgil, A., Parihar, J.: Evapotranspiration using MODIS data and limited
884 ground observations over selected agroecosystems in India, *Int. J. Remote Sens.*, 28(10),
885 2091-2110, <https://doi.org/10.1080/01431160600935620>, 2007.
- 886 Mallick, K., Bhattacharya, B. K., Rao, V. U. M., Reddy, D.R., Banerjee, S., Venkatesh, H. ,
887 Pandey, V., Kar, G., Mukherjee, J., Vyas, S., Gadgil, A.S., Patel, N.K.: Latent heat flux
888 estimation in clear sky days over Indian agroecosystems using noontime satellite remote
889 sensing data, *Agric For Meteorol*, 149(10), 1646-1665,
890 <https://doi.org/10.1016/j.agrformet.2009.05.006>, 2009.
- 891 Mallick, K., Boegh, E., Trebs, I., Alfieri, J., Kustas, W., Prueger, J., Niyogi, D., Das, N., Drewry,
892 D., Hoffmann, L. and Jarvis, A.: Reintroducing radiometric surface temperature into the
893 Penman-Monteith formulation, *Water Resour. Res.*, 51(8), 6214 – 6243,
894 <https://doi.org/10.1002/2014WR016106>, 2015a.
- 895 Mallick, K., Jarvis, A., Boegh, E., Fisher, J., Drewry, D., Tu, K., Hook, S., Hulley, G., Ardö, J.,
896 Beringer, J., Arain, A. and Niyogi, D.: A Surface Temperature Initiated Closure (STIC) for
897 surface energy balance fluxes, *Remote Sens. Environ.*, 141, 243 – 261,
898 <https://doi.org/10.1016/j.rse.2013.10.022>, 2014.
- 899 Mallick, K., Jarvis, A., Wohlfahrt, G., Kiely, G., Hirano, T., Miyata, A., Yamamoto, S., and
900 Hoffmann, L.: Components of near-surface energy balance derived from satellite soundings –
901 Part 1: Noontime net available energy, *Biogeosci.*, 12, 433–451, [https://doi.org/10.5194/bg-](https://doi.org/10.5194/bg-12-433-2015)
902 [12-433-2015](https://doi.org/10.5194/bg-12-433-2015), 2015.
- 903 Mallick, K., Toivonen, E., Trebs, I., Boegh, E., Cleverly, J., Eamus, D., Koivusalo, H., Drewry,
904 D., Arndt, S., Griebel, A., Beringer, J. and Garcia, M.: Bridging Thermal Infrared Sensing and
905 Physically-Based Evapotranspiration Modeling: From Theoretical Implementation to
906 Validation Across an Aridity Gradient in Australian Ecosystems, *Water Resour. Res.*, 54(5),
907 3409 – 3435, <https://doi.org/10.1029/2017WR021357>, 2018a.
- 908 Mallick, K., Trebs, I., Boegh, E., Giustarini, L., Schlerf, M., Drewry, D., Hoffmann, L., von
909 Randow, C., Kruijt, B., Araùjo, A., Saleska, S., Ehleringer, J., Domingues, T., Ometto, J.,



- 110 Nobre, A., de Moraes, O., Hayek, M., Munger, J. and Wofsy, S.: Canopy-scale biophysical
111 controls of transpiration and evaporation in the Amazon Basin, *Hydrol. Earth Syst. Sci.*, 20,
112 4237–4264, doi:10.5194/hess-20-4237-2016, 2016.
- 113 Mallick, K., Wandera, L., Bhattarai, N., Hostache, R., Kleniewska, M. and Chormanski, J.: A
114 Critical Evaluation on the Role of Aerodynamic and Canopy–Surface Conductance
115 Parameterization in SEB and SVAT Models for Simulating Evapotranspiration: A Case Study
116 in the Upper Biebrza National Park Wetland in Poland, *Water*, 10(12), 1753,
117 <https://doi.org/10.3390/w10121753>, 2018b.
- 118 Maltese, A., Bates, P., Capodici, F., Cannarozzo, M., Ciraolo, G. and La Loggia, G.: Critical
119 analysis of thermal inertia approaches for surface soil water content retrieval, *Hydrol. Sci. J.*,
120 58(5), 1144–1161, <https://doi.org/10.1080/02626667.2013.802322>, 2013.
- 121 Martel, M., Glenn, A., Wilson, H. and Kröbel, R.: Simulation of actual evapotranspiration from
122 agricultural landscapes in the Canadian Prairies, *J. Hydrol. Reg. Stud.*, 15, 105 – 118,
123 <https://doi.org/10.1016/j.ejrh.2017.11.010>, 2018.
- 124 Matheny, A., Bohrer, G., Stoy, P., Baker, I., Black, A., Desai, A., Dietze, M., Gough, C., Ivanov,
125 V., Jassal, R., Novick, K., Schäfer, K. and Verbeeck, H.: Characterizing the diurnal patterns
126 of errors in the prediction of evapotranspiration by several land-surface models: An NACP
127 analysis, *J. Geophys. Res. Biogeosci.*, 119 (7), 1458 – 1473,
128 <https://doi.org/10.1002/2014JG002623>, 2014.
- 129 Minasny, B. & Hartemink, A. E.: Predicting soil properties in the tropics. *Earth-Science Rev.*, 1
130 – 2, 52 – 62, <https://doi.org/10.1016/j.earscirev.2011.01.005>, 2011.
- 131 Monteith, J & Unsworth, M.: *Principles of Environmental Physics: Plants, Animals, and the*
132 *Atmosphere*, Fourth Edition, 1–401, 2013.
- 133 Moran, M. S., Jackson, R. D., Raymond, L. H., Gay, L. W. and Slater, P. N.: Mapping surface
134 energy balance components by combining landsat thematic mapper and ground-based
135 meteorological data, *Remote Sens. Environ.*, 30, 77 – 87, [https://doi.org/10.1016/0034-](https://doi.org/10.1016/0034-4257(89)90049-7)
136 [4257\(89\)90049-7](https://doi.org/10.1016/0034-4257(89)90049-7), 1989.
- 137 Morisson, R., Angadi, S. S., Cooper, H. M., Evans, J. G., Rees, G., Sekhar, M., Taylor, C.,
138 Tripathi, S. N. and Turner, A. G. : Energy and carbon dioxide fluxes, meteorology and soil
139 physics observed at INCOMPASS land surface stations in India, 2016 to 2017, NERC



- 940 Environmental Information Data Centre, doi:10.5285/78c64025-1f8d-431cbdeb-
941 e69a5877d2ed, 2019b.
- 942 Morisson, R., Angadi, S. S., Cooper, H. M., Evans, J., Rees, G., Sekhar, M., Taylor, C., Tripathi,
943 S. N. and Turner, A. G. : High temporal resolution meteorology and soil physics observations
944 from INCOMPASS land surface stations in India, 2016 to 2018, NERC Environmental
945 Information Data Centre, doi:10.5285/c5e72461-c61f-4800-8bbf-95c85f74c416, 2019a.
- 946 Murray, T. and Verhoef, A.: Moving towards a more mechanistic approach in the determination
947 of soil heat flux from remote measurements, *Agric. For. Meteorol.*, 147(1-2), 80 – 87,
948 <https://doi.org/10.1016/j.agrformet.2007.06.009>, 2007.
- 949 Norman, J., Anderson, M., Kustas, W., French, A., Mecikalski, J., Torn, R., Diak, G., Schmugge,
950 T. and Tanner, B.: Remote sensing of surface energy fluxes at 10¹-m pixel resolutions, *Water*
951 *Resour. Res.* 39(8), <https://doi.org/10.1029/2002WR001775>, 2003.
- 952 Purdy, A., Fisher, J., Goulden, M. and Famiglietti, J.: Ground heat flux: An analytical review of
953 6 models evaluated at 88 sites and globally, *J. Geophys. Res.: Biogeosci.*, 121(12), 3045 –
954 3059, <https://doi.org/10.1002/2016JG003591>, 2016.
- 955 Raja, P., Singh, M., Singh, N., and Sinha, N.K.: Photosynthesis and Biomass studies in *Lasiurus*
956 *indicus* of Chandan Grassland in Thar Desert, XXIII International Grassland Conference, New
957 Delhi, Volume: IGC 2015, 2015.
- 958 Santanello, J. and Friedl, M.: Diurnal Covariation in Soil Heat Flux and Net Radiation, *J. Appl.*
959 *Meteorol.*, 42(6), 851 – 862, [https://doi.org/10.1175/1520-
960 0450\(2003\)042<0851:DCISHF>2.0.CO;2](https://doi.org/10.1175/1520-0450(2003)042<0851:DCISHF>2.0.CO;2), 2003.
- 961 Sauer T.J. and Horton, R.: Soil Heat flux, *Micrometeorology in Agricultural Systems*, Agronomy
962 Monograph no. 47, American Society of Agronomy, Crop Science Society of America, Soil
963 Science Society of America, 677 S. Segoe Rd., Madison, WI 53711, USA, 2005.
- 964 Schaaf, C., Gao, F., Strahler, A., Lucht, W., Li, X., & Tsang, T., Trugnell, N. C., Zhang, X., Jin,
965 Y., Muller, J., Lewis, P., Barnsley, M., Hobson, P., Disney, M., Roberts, G., Dunderdale, M.,
966 Doll, C., d'Entremont, R. P., Hu, B., Liang, S., Privette, J. L. and Roy, D. : First operational
967 BRDF, albedo nadir reflectance products from MODIS, *Remote Sens. Environ.*, 83 (1-2), 135-
968 148, doi:10.1016/s0034-4257(02)00091-3, 2002.



- 969 Schymanski, S. J., Breitenstein, D., and Or, D.: Technical note: An experimental set-up to measure
970 latent and sensible heat fluxes from (artificial) plant leaves, *Hydrol. Earth Syst. Sci.*, 21, 3377–
971 3400, <https://doi.org/10.5194/hess-21-3377-2017>, 2017.
- 972 Singh, A.: *Integrated Water Management: Water and Plant Growth*, 1–16, 2007.
- 973 Stoy, P., Mauder, M., Foken, T., Marcolla, B., Boegh, E., Ibrom, A., Arain, M., Arneth, A.,
974 Aurela, M., Bernhofer, C., Cescatti, A., Dellwik, E., Duce, P., Gianelle, D., van Gorsel, E.,
975 Kiely, G., Knohl, A., Margolis, H., McCaughey, H., Merbold, L., Montagnani, L., Papale, D.,
976 Reichstein, M., Saunders, M., Serrano-Ortiz, P., Sottocornola, M., Spano, D., Vaccari, F. and
977 Varlagin, A.: A data-driven analysis of energy balance closure across FLUXNET research
978 sites: The role of landscape scale heterogeneity, *Agric. For. Meteorol.*, 171 – 172, 137 – 152,
979 <https://doi.org/10.1016/j.agrformet.2012.11.004>, 2013.
- 980 Su, Z.: The Surface Energy Balance System (SEBS) for estimation of turbulent heat fluxes,
981 *Hydrol. Earth Syst. Sci.*, 6, 85–100, doi:10.5194/hess-6-85-2002, 2002.
- 982 Tian, L., Zhang, Y., & Zhu, J.: Decreased surface albedo driven by denser vegetation on the
983 Tibetan Plateau, *Environ. Res. Lett.*, 9(10), 104001, doi:10.1088/1748-9326/9/10/104001,
984 2014.
- 985 Trebs, I., Mallick, K., Bhattarai, N., Sulis, M., Cleverly, J., Woodgate, W., Silberstein, R., Najera,
986 H.-N., Beringer, J., Meyer, W. S., Su, Z., and Boulet, G.: The role of aerodynamic resistance
987 in thermal remote sensing-based evapotranspiration models, *Remote Sens. Environ.*, 264,
988 112602, doi:10.1016/j.rse.2021.112602, 2021
- 989 Tsuang, B.: Ground Heat Flux Determination according to Land Skin Temperature Observations
990 from *in-situ* Stations and Satellites, *J. Hydrometeorol.*, 6(4), 371 – 390,
991 <https://doi.org/10.1175/JHM425.1>, 2005.
- 992 Turner, A., Bhat, G., Martin, G., Parker, D., Taylor, C., Mitra, A., Tripathi, S., Milton, S.,
993 Rajagopal, E., Evans, J., Morrison, R., Pattnaik, S., Sekhar, M., Bhattacharya, B., Madan, R.,
994 Govindankutty, M., Fletcher, J., Willetts, P., Menon, A. and Marsham, J.: Interaction of
995 convective organization with monsoon precipitation, atmosphere, surface and sea: The 2016
996 INCOMPASS field campaign in India, *Q. J. R. Meteorolog. Soc.*, 1–25,
997 <https://doi.org/10.1002/qj.3633>, 2019.
- 998 Van Dijk, A.I.J.M., Gash, J.H., Gorsel, E.V., Blanken, P.D., Cescatti, A., Emmel, C., Gielen, B.,
999 Harman, I.N., Kiely, G., Merbold, L., Montagnani, L., Moors, E., Sottocornola, M., Varlagin,



- 1000 A., Williams, C.A., Wohlfahrt, G.: Rainfall interception and the coupled surface water and
1001 energy balance, *Agric For Meteorol.*, 214 – 215, 402 – 415,
1002 <https://doi.org/10.1016/j.agrformet.2015.09.006>, 2015.
- 1003 Van Genuchten, M.: A Closed-form Equation for Predicting the Hydraulic Conductivity of
1004 Unsaturated Soils, *Soil Sci. Soc. Am. J.*, 44(5), 892,
1005 <https://doi.org/10.2136/sssaj1980.03615995004400050002x>, 1980.
- 1006 Venturini, V., Islam, S. and Rodriguez, L.: Estimation of evaporative fraction and
1007 evapotranspiration from MODIS products using a complementary based model, *Remote Sens.*
1008 *Environ.*, 112(1), 132 – 141, doi:10.1016/j.rse.2007.04.014, 2008.
- 1009 Verhoef, A., Ottlé, C., Cappelaere, B., Murray, T., Saux-Picart, S., Zribi, M., Maignan, F.,
1010 Boulain, N., Demarty, J. and Ramier, D.: Spatio-temporal surface soil heat flux estimates from
1011 satellite data; results for the AMMA experiment at the Fakara (Niger) supersite, *Agric. For.*
1012 *Meteorol.*, 154-155, 55 – 66, doi:10.1016/j.agrformet.2011.08.003, 2012.
- 1013 Verhoef, A.: Remote estimation of thermal inertia and soil heat flux for bare soil, *Agric. For.*
1014 *Meteorol.*, 123(3-4), 221 – 236, doi:10.1016/j.agrformet.2003.11.005, 2004.
- 1015 Wan, Z.: New refinements and validation of the collection-6 MODIS land-surface
1016 temperature/emissivity product, *Remote Sens. Environ.*, 140, 36 – 45,
1017 doi:10.1016/j.rse.2013.08.027, 2014.
- 1018 Wang, S., Yang, Y., Luo, Y., and Rivera, A.: Spatial and seasonal variations in evapotranspiration
1019 over Canada's landmass, *Hydrol. Earth Syst. Sci.*, 17, 3561–3575, doi:10.5194/hess-17-3561-
1020 2013, 2013.
- 1021 Wilson, K., Goldstein, A., Falge, E., Aubinet, M., Baldocchi, D., Berbigier, P., Bernhofer, C.,
1022 Ceulemans, R., Dolman, H., Field, C., Grelle, A., Ibrom, A., Law, B., Kowalski, A., Meyers,
1023 T., Moncrieff, J., Monson, R., Oechel, W., Tenhunen, J., Valentini, R. and Verma, S.: Energy
1024 balance closure at FLUXNET sites, *Agric. For. Meteorol.*, 113(1-4), 223 – 243,
1025 doi:10.1016/S0168-1923(02)00109-0, 2002.
- 1026 Winter, J. and Eltahir, E.: The Sensitivity of Latent Heat Flux to Changes in the Radiative Forcing:
1027 A Framework for Comparing Models and Observations, *J. Clim.*, 23(9), 2345-2356,
1028 doi:10.1175/2009JCLI3158.1, 2010.
- 1029 Xue, J. & Su, B.: Significant Remote Sensing Vegetation Indices: A Review of Developments
1030 and Applications. *J. Sens.*, 1-17, doi:10.1155/2017/1353691, 2017.



1031 **Appendix A**

1032 **Table A1: A list of symbols, their descriptions and units used in the present study**

Attributes	Symbol	Description
Temperature	T_A	Air temperature ($^{\circ}\text{C}$)
	T_{Max}	Maximum air temperature ($^{\circ}\text{C}$)
	T_{Min}	Minimum air temperature ($^{\circ}\text{C}$)
	T_D	Air dew-point temperature ($^{\circ}\text{C}$)
	T_{STA}	point-scale soil temperature amplitude
	ΔT_s	noon-night LST difference ($^{\circ}\text{C}$)
	T_{ST}	Soil temperature ($^{\circ}\text{C}$)
	T_s	Land surface temperature (LST) ($^{\circ}\text{C}$)
Humidity, vapor pressures	R_H	Relative humidity (%)
	e_A	Atmospheric vapor pressure at the level of T_A measurement (hPa)
	e_A^*	Saturation vapor pressure at the level of T_A measurement (hPa)
	e_s^*	Saturation vapor pressure at surface (hPa)
	D_A	Atmospheric vapor pressure deficit at the level of T_A measurement (hPa)
Radiation	R_G	Downwelling shortwave radiation (or global radiation) (W m^{-2})
	R_R	Upwelling or reflected shortwave radiation (W m^{-2})
	$R_{L\downarrow}$	Downwelling longwave radiation (W m^{-2})
	$R_{L\uparrow}$	Upwelling longwave radiation (W m^{-2})
	τ_{sw}	Atmospheric transmissivity for shortwave radiation (unitless)



	α_R	Broadband shortwave surface albedo (unitless)
SEB components	LE_i	Latent heat flux ($W\ m^{-2}$); subscript 'i' signifies 'instantaneous'
	H_i	Sensible heat flux ($W\ m^{-2}$); subscript 'i' signifies 'instantaneous'
	G_i	Ground heat flux ($W\ m^{-2}$); subscript 'i' signifies 'instantaneous'
	R_{Ni}	Net radiation ($W\ m^{-2}$); subscript 'i' signifies 'instantaneous'
	ϕ	Net available energy ($W\ m^{-2}$); i.e., $R_N - G$
MV2007 model	A	Ecosystem-scale surface soil temperature amplitude ($^{\circ}C$)
	T_{Sd}	Daytime T_S ($^{\circ}C$)
	T_{Sn}	Nighttime T_S ($^{\circ}C$)
	ω	Angular frequency ($rad\ s^{-1}$)
	ϕ'_n	Phase shift of the n^{th} soil surface temperature harmonic (rad)
	Δ	Shape parameter (unitless)
	S_r	Relative soil moisture saturation ($m^3\ m^{-3}$)
	f_s	Sand fraction (unitless)
	θ_{fc}	Soil water content at field capacity ($m^3\ m^{-3}$)
	θ_{wp}	Soil water content at permanent wilting point ($m^3\ m^{-3}$)
	θ^*	Soil porosity ($cm^3\ cm^{-3}$)
	J_s	Summation of harmonic terms of soil surface temperature (K)
	Υ'	Soil textural parameter (unitless)
	Γ	Soil thermal inertia ($J\ K^{-1}\ m^{-2}\ s^{-0.5}$)
τ_0	Thermal inertia of air-dry soil ($J\ K^{-1}\ m^{-2}\ s^{-0.5}$)	
τ^*	Thermal inertia of saturated soil ($J\ K^{-1}\ m^{-2}\ s^{-0.5}$)	



	t'	Time of satellite overpass (seconds)
	Δt	Time offset between the canopy composite temperature and the below-canopy soil surface temperature (seconds)
	κ	Total number of harmonics used (unitless)
	f_c	Vegetation fraction (unitless)
	θ	Volumetric soil moisture (cm cm^{-3})
Clear-sky R_{Ni} model	R_{ns}	Net shortwave radiation (W m^{-2})
	R_{nl}	Net long wave radiation (W m^{-2})
	G_{sc}	Solar constant (1367 W m^{-2})
	β_e	Sun elevation angle ($^\circ$).
	ϵ_s	Infrared surface emissivity (unitless)
	ϵ_a	Atmospheric emissivity (unitless)
	E	Eccentricity correction factor due to variation in Sun-Earth distance (unitless)
	M	Aggregated moisture availability (0-1)
	g_A	Aerodynamic conductance (m s^{-1})
	g_s	Canopy-surface conductance (m s^{-1})
	T_0	Aerodynamic temperature (or source/sink height temperature) ($^\circ\text{C}$)
	T_{0D}	Dewpoint temperature at the source/sink height ($^\circ\text{C}$)
	Λ	Evaporative fraction (unit less)
	e_0	Vapor pressure at the source/sink height (hPa)
	e_0^*	Saturation vapor pressure at the source/sink height (hPa)



STIC-TI model	D_0	Vapor pressure deficit at source/sink height (hPa)
	s_1	Psychrometric slope of vapor pressure and temperature between (T_{0D} - T_D) versus ($e_0 - e_A$) (h Pa K^{-1})
	s_2	Psychrometric slope of vapor pressure and temperature between (T_S - T_D) versus ($e_s^* - e_A$) (h Pa K^{-1})
	s_3	Psychrometric slope of vapor pressure and temperature between (T_{0D} - T_D) versus ($e_s^* - e_A$).
	κ	Ratio between ($e_0^* - e_A$) and ($e_s^* - e_A$) (unitless)
	s	Slope of saturation vapor pressure vs. temperature curve (h Pa K^{-1})
	α	Priestley-Taylor coefficient (unitless)
Ancillary meteorological variables	U	Wind speed at 8 m height (m s^{-1})
	u^*	Friction velocity (m s^{-1})
Constants	P	Precipitation (mm d^{-1})
	γ	Psychrometric constant (h Pa K^{-1})
	c_p	Specific heat capacity of air at constant pressure ($\text{MJ kg}^{-1} \text{K}^{-1}$)
	ρ	Density of air (Kg m^{-3})
	σ	Stefan–Boltzmann constant ($5.67 \times 10^{-8} \text{ Wm}^{-2}\text{K}^{-4}$)

1033

1034

1035



1036 **Table A2:** Summary of instruments used, height or depth and period of measurements, measured
 1037 variables at nine EC flux tower sites

Type of primary instruments used for in situ data recording at flux tower sites	Measurement Height/ Depth (m) at different sites	Measured variables
Net radiometer	<ul style="list-style-type: none"> • 3m (IND-Naw, IND-Jai, IND-Sam) • 15m (AU-Ade) • 12.2m (AU-ASM) • 23m (AU-How) 2m (US-Ton, US-Var) 	Four radiation flux components: shortwave incoming (R_G) and outgoing (R_R); longwave incoming ($R_{L\downarrow}$) and outgoing ($R_{L\uparrow}$)
EC assembly with IRGA (Infrared Gas Analyzer), three-dimensional sonic anemometer, TC probe	<ul style="list-style-type: none"> • 8m (IND-Naw; IND-Jai; IND-Sam) • 4.5m (IND-Dha) • 15m (AU-Ade) • 11.6m (AU-ASM) • 23m (AU-How) • 2m (US-Ton, US-Var) 	High response wind vectors (u , v and w), sonic temperature, and CO_2 - water vapor mass at 10/20 Hz frequency
Humidity and temperature probe	<ul style="list-style-type: none"> • 8m (IND-Naw, IND-Jai, IND-Sam) • 4.5m (IND-Dha) • 15m (AU-Ade), 11.6m (AU-ASM) • 23m (AU-How), 70m (AU-How) • 2m (US-Ton, US-Var) 	T_A and R_H
Soil temperature probe	<ul style="list-style-type: none"> • -0.1m (IND-Dha) • -0.15m (AU-Ade) • (-0.02, -0.06m) (AU-ASM) • -0.08m (AU-How) • -0.02m, -0.04m, -0.08m, and -0.16m (US-Ton, US-Var) 	T_{ST}
Soil heat flux plates	<ul style="list-style-type: none"> • Ground, 0.1 m (IND-Dha) • Ground, -0.15 m (AU-Ade) • Ground, -0.08 m (AU-ASM) • Ground, -0.15 m (AU-How) • -0.01m (US-Ton, US-Var) 	Soil heat flux (G)

1038 **Appendix B**

1039 **B1: Clear-sky instantaneous net radiation (R_{Ni}) model**

1040 Net radiation (R_N) is defined as the difference between the incoming and outgoing radiation fluxes,
 1041 which includes both longwave and shortwave radiation at the surface of earth.



1042 Terrestrial R_N has four components: downwelling and upwelling shortwave radiation (R_G and R_R),
1043 downwelling and upwelling longwave radiation ($R_{L\downarrow}$ and $R_{L\uparrow}$), respectively.

$$R_N = (R_G - R_R) + (R_{L\downarrow} - R_{L\uparrow}) \quad (\text{B1})$$

1044 Out of these four terms mentioned in eq.(B1), R_G and $R_{L\downarrow}$ are dependent on various factors such
1045 as geographic location, season, cloudiness, aerosol loading, atmospheric water vapor content and
1046 less on surface properties. On the other hand, the upwelling radiations in eq. (B1) strongly depends
1047 on the surface properties such as surface reflectance and emittance, land surface temperature, and
1048 soil water content (Zerefos and Bais, 2013).

1049 Instantaneous net radiation (R_{Ni}) can be derived using eq. B2 as follows (Mallick et al., 2007):

$$R_{Ni} = R_{ns} - R_{nl} \quad (\text{B2})$$

$$R_{ns} = (1 - \alpha_R) R_G \quad (\text{B3})$$

$$R_{nl} = R_{L\downarrow} - R_{L\uparrow} \quad (\text{B4})$$

1050 Where, R_{ns} is net shortwave radiation (W m^{-2}), R_{nl} is net longwave radiation (W m^{-2}).and α_R is
1051 the broadband surface albedo shortwave spectrum.

1052 A WMO (World Meteorological Organization) shortwave radiation model (Cano et al.,1986)
1053 calibrated over Indian conditions (Mallick et al., 2007, 2009) was used to compute R_G using the
1054 following equation:

$$R_G = \tau_{sw} G_{sc} E (\sin\beta_e)^{1.15} \quad (\text{B5})$$

1055 Where, τ_{sw} is the is the global clear sky transmissivity for the shortwave radiation (0.7), G_{sc} is the
1056 solar constant (1367 Wm^{-2}), ε is the eccentricity correction factor due to variation in Sun-Earth
1057 distance and β_e is the sun elevation in degrees.

1058 $R_{L\downarrow}$ at any instance was calculated as follows:

$$R_{L\downarrow} = \varepsilon_a \sigma (273.14 + T_A)^4 \quad (\text{B6})$$



1059 Where, σ is the Stefan–Boltzmann constant ($5.67 \times 10^{-8} \text{ W m}^{-2} \text{ K}^{-4}$); T_A is the air temperature ($^{\circ}\text{C}$);
1060 ϵ_a is the atmospheric emissivity.

1061 Atmospheric emissivity (ϵ_a) was computed using the following equation (Bastiaanssen et
1062 al., 1998):

$$\epsilon_a = 0.85 - \ln \tau_{\text{sw}}^{0.09} \quad (\text{B7})$$

1063 $R_{L\uparrow}$ at any particular instance was calculated as follows:

$$R_{L\uparrow} = \epsilon_s \sigma (273.14 + T_s)^4 \quad (\text{B8})$$

1064 Where, ϵ_s is the surface emissivity in thermal infrared (8 – 14 μm) spectrum and T_s is the land
1065 surface temperature ($^{\circ}\text{C}$).

1066 **B2: Evaluation of STIC-TI R_{Ni}**

1067 Comparison of the clear-sky R_{Ni} estimates with respect to *in situ* measurements revealed RMSE in
1068 R_{Ni} to the order of 27 – 72 W m^{-2} , MAPD 8 – 24%, BIAS (-67) – 50 W m^{-2} , and R^2 varying from
1069 0.62– 0.90 across all the sites (Fig. B2, Table B2). Among the nine sites, a consistent
1070 underestimation of R_{Ni} was noted in IND-Dha, US-Ton, and US-Var (with BIAS of -23 W m^{-2} , -
1071 61 W m^{-2} and -67 W m^{-2}), whereas substantial overestimation of R_{Ni} was found in IND-Sam, IND-
1072 Naw, and AU-ASM with a BIAS of 50 W m^{-2} , 37 W m^{-2} and 43 W m^{-2} , respectively (Table B2).

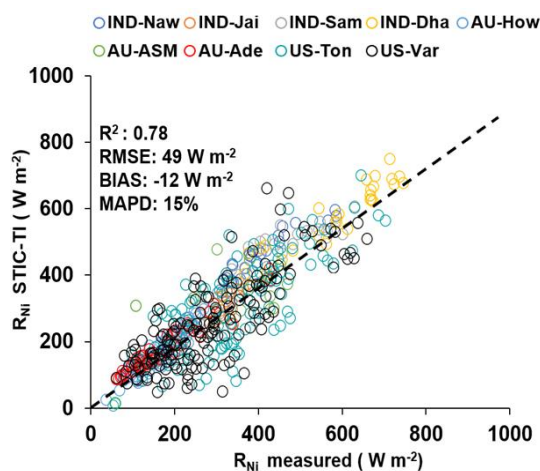


Figure B2: Validation of STIC-TI derived R_{Ni} estimates with respect to *in situ* measurements in different ecosystems. The regression equation between modeled versus *in-situ* R_{Ni} is, R_{Ni} (STIC-TI) = $0.78R_{Ni}$ (tower) + 58.92.

1073 **Table B2:** Performance evaluation statistics of clear-sky R_{Ni} estimates in nine different
 1074 agroecosystems

Sites	Error statistics of clear-sky R_{Ni} model estimates			
	R^2	BIAS ($W m^{-2}$)	RMSE ($W m^{-2}$)	MAPD (%)
IND-Jai	0.81	-9	32	8
IND-Naw	0.81	37	56	12
IND-Dha	0.81	-23	42	9
IND-Sam	0.64	50	67	15
US-Ton	0.68	-61	69	21
US-Var	0.62	-67	72	24
Au-How	0.87	7	27	15
AU-ASM	0.88	43	50	14
AU-Ade	0.90	11	27	16



1075 **Appendix C**

1076 **C1: Estimating SEB fluxes using STIC1.2 analytical model and thermal remote sensing data**

1077 STIC1.2 (Mallick et al., 2014, 2015a,b, 2016, 2018a) is a one-dimensional physically based SEB
1078 model and is based on the integration of satellite LST observations into the Penman–Monteith
1079 Energy Balance (PMEB) equation (Monteith, 1965). In STIC1.2, the vegetation–substrate
1080 complex is considered as a single slab. Therefore, the aerodynamic conductances from individual
1081 air-canopy and canopy-substrate components is regarded as an ‘effective’ aerodynamic
1082 conductance (g_A), and surface conductances from individual canopy (stomatal) and substrate
1083 complexes is regarded as an ‘effective’ canopy-surface conductance (g_S) which simultaneously
1084 regulate the exchanges of sensible and latent heat fluxes (H and LE) between surface and
1085 atmosphere. One of the fundamental assumptions in STIC1.2 is the first order dependence of these
1086 two critical conductances on M through T_s . Such an assumption enabled an integration of satellite
1087 LST in the PMEB model (Mallick et al., 2016). The common expression for LE and H according
1088 to the PMEB equation is as follows:

$$LE = \frac{s\phi + \rho c_P g_A D_A}{s + \gamma \left(1 + \frac{g_A}{g_S}\right)} \quad (C6)$$

$$H = \frac{\gamma\phi \left(1 + \frac{g_A}{g_S}\right) - \rho c_P g_A D_A}{s + \gamma \left(1 + \frac{g_A}{g_S}\right)} \quad (C7)$$

1089 In the above equations, the two biophysical conductances (g_A and g_S) are unknown and the
1090 STIC1.2 methodology is based on finding analytical solutions for the two unknown conductances
1091 to directly estimate LE (Mallick et al., 2016, 2018a). The need for such analytical estimation of
1092 these conductances is motivated by the fact that g_A and g_S can neither be measured at the canopy
1093 nor at larger spatial scales, and there is no universally agreed appropriate model of g_A and g_S that
1094 currently exists (Matheny et al., 2014; van Dijk et al., 2015). By integrating T_s with standard SEB
1095 theory and vegetation biophysical principles, STIC1.2 formulates multiple state equations in order



1096 to eliminate the need to use the empirical parameterizations of the g_A and g_S and also to bypass the
1097 scaling uncertainties of the leaf-scale conductance functions to represent the canopy-scale
1098 attributes. The state equations for the conductances are expressed as a function of those variables
1099 that are mostly available as remote sensing observations and weather forecasting models. In the
1100 state equations, a direct connection to T_S is established by estimating M as a function of T_S . The
1101 information of M is subsequently used in the state equations of conductances, aerodynamic
1102 variables (aerodynamic temperature, aerodynamic vapor pressure), and evaporative fraction,
1103 which is eventually propagated into their analytical solutions. M is a unitless quantity, which
1104 describes the relative wetness (or dryness) of a surface and also controls the transition from
1105 potential to actual evaporation; which implies $M \rightarrow 1$ under saturated surface conditions and $M \rightarrow 0$
1106 under extremely dry conditions. Therefore, M is critical for providing a constraint against which
1107 the conductances are estimated. Since T_S is extremely sensitive to the surface moisture variations,
1108 it is extensively used for estimating M in a physical retrieval scheme (detail in Appendix A3 of
1109 Bhattarai et al., 2018; Mallick et al., 2016, 2018a). It is hypothesized that linking M with the
1110 conductances will simultaneously integrate the information of T_S into the PMEB model. To
1111 illustrate, we express the state equations by symbols, $sv_1 = f\{c_1, c_2, c_3, v_1, v_2, v_3, v_4, sv_3, sv_5\}$; sv_2
1112 $= f\{v_4, sv_1, sv_5, sv_6\}$; $sv_3 = f\{c_3, v_3, v_4, sv_4, sv_5\}$; $sv_4 = f\{c_3, v_3, sv_1, sv_2, sv_7, sv_8\}$. Here, f , sv , v ,
1113 and c denote the function, state variables, input variables (5 input variables; radiative and
1114 meteorological), and constants (3 constants), respectively. Here sv_1 to sv_4 are g_A , g_S , aerodynamic
1115 temperature (T_0), evaporative fraction (Λ), and sv_8 is M . Given the estimates of M , net radiative
1116 energy ($R_{Ni} - G_i$), T_A , R_H , the four state equations are solved simultaneously to derive analytical
1117 solutions for the four state variables and to produce a surface energy balance “closure” that is
1118 independent of empirical parameterizations for g_A , g_S , T_0 , and Λ . However, the analytical solutions
1119 to the four state equations contain three accompanying unknown state variables (effective vapor
1120 pressures at source/sink height, and Priestley-Taylor variable), and as a result there are four
1121 equations with seven unknowns. Consequently, an iterative solution was found to determine the
1122 three additional unknown variables as detailed in this section above and also described in Mallick
1123 et al. (2016, 2018a) and Bhattarai et al. (2018). The state equations of STIC are given below.



$$g_A = \frac{\phi}{\rho_{CP} \left[(T_0 - T_A) + \left(\frac{e_0 - e_A}{\gamma} \right) \right]} \quad (C1)$$

$$g_S = g_A \frac{(e_0 - e_A)}{(e_0^* - e_0)} \quad (C2)$$

$$T_0 = T_A + \left(\frac{e_0 - e_A}{\gamma} \right) \left(\frac{1 - \Lambda}{\Lambda} \right) \quad (C3)$$

$$\Lambda = \frac{2\alpha s}{2s + 2\gamma + \gamma \frac{g_A}{g_S} (1 + M)} \quad (C4)$$

1124 Detailed derivations of these four state equations are given in Mallick et al. (2016). Given the
1125 values of M , R_N , G , T_A , and R_H or e_A , the four state equations can be solved simultaneously to
1126 derive analytical solutions for the four unobserved variables and to simultaneously produce a
1127 ‘closure’ of the PMEB model that is independent of empirical parameterizations for both g_A and
1128 g_S . However, the analytical solutions to the four state equations contain three accompanying
1129 unknowns; e_0 (vapor pressure at the source/sink height), e_0^* (saturation vapor pressure at the
1130 source/sink height), and Priestley-Taylor coefficient (α), and as a result there are four equations
1131 with seven unknowns. Consequently, an iterative solution was needed to determine the three
1132 unknown variables (as described in Appendix A2 in Mallick et al. 2016). Once the analytical
1133 solutions of g_A and g_S are obtained, both variables are returned into eq. (13) to directly estimate
1134 LE.

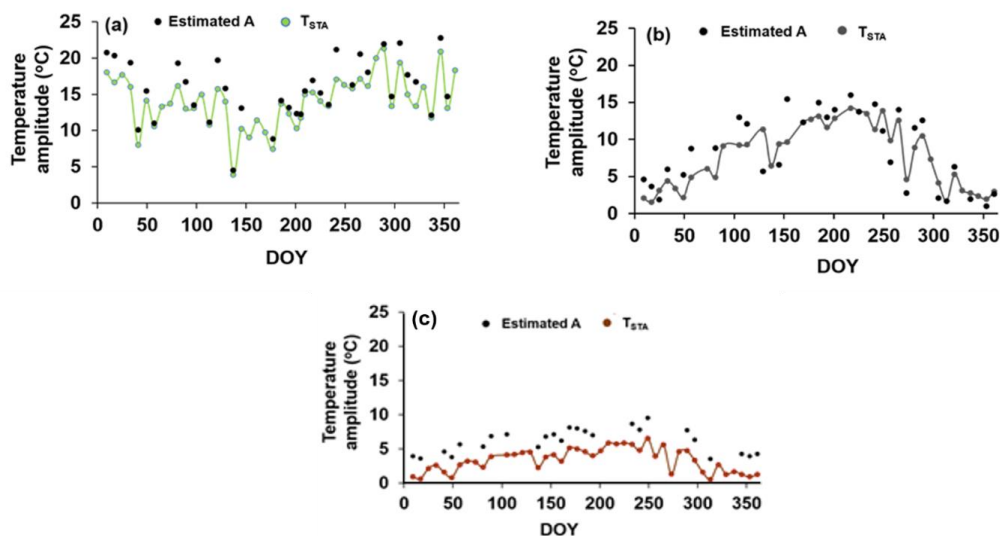
1135 In STIC-TI, an initial value of α was assigned as 1.26; initial estimates of e_0^* were obtained from
1136 T_S through temperature-saturation vapour pressure relationship, and initial estimates of e_0 were
1137 obtained from M as, $e_0 = e_A + M(e_0^* - e_A)$. Initial T_{0D} and M were estimated according to
1138 Venturini et al. (2008) as described in section 3.2, and initial estimation of G was performed from
1139 initial M using the equation sets eq. (2) – eq. (11). With the initial estimates of these variables;
1140 first estimate of the conductances, T_0 , Λ , H , and LE were obtained. The process was then iterated
1141 by updating e_0^* , D_0 , e_0 , T_{0D} , M , and α (using eq. A9, A10, A11, A17, A16 and A15 in Mallick et
1142 al., 2016), with the first estimates of g_S , g_A , T_0 , and LE, and re-computing G , ϕ , g_S , g_A , T_0 , Λ , H ,
1143 and LE in the subsequent iterations with the previous estimates of e_0^* , e_0 , T_{0D} , M , and α until the



1144 convergence of LE was achieved. Stable values of G, conductances, LE, H, T_0 , e_0^* , e_0 , T_{0D} , M, and
1145 α were obtained within ~25 iterations. The inputs needed for computation of LE_i (eq.C6) are air
1146 temperature (T_A), land surface temperature (T_S), relative humidity (R_H), net radiation (R_{Ni}) and
1147 soil heat flux (G_i).

1148 Appendix D

1149 The temporal variation of estimated A and T_{STA} is shown in Fig. D1. The annual variations of T_{STA}
1150 in different ecosystem was found to be within the ranges of 1 - 4°C.



1151
1152 **Figure D1:** Temporal variation of A and T_{STA} in (a) AU-ASM (2013), (b) US-Ton (2014), (c) US-
1153 Var (2014).

1154
1155
1156
1157



1158 **Appendix E**

1159 **Table E1:** Soil textural properties and their values used in the present study (Murray and Verhoef,
1160 2007; Minasny et al., 2011; Anderson et al., 2007)

Soil texture	Water retention Shape parameter (δ)	Field capacity (vol/vol) (%) θ_{fc}	Wilting point (vol/vol) (%) θ_{wp}	Sand fraction (f_s)	Saturated soil moisture (vol/vol) (%) θ^*
Sand	2.77	10	5	0.92	43
Loamy Sand	2.39	12	5	0.82	41
Sandy loam	2.27	18	8	0.58	41
Loam	2.20	28	14	0.43	43
Silty loam	2.22	31	11	0.17	45
Sandy clay loam	2.17	27	17	0.58	39
Clay loam	2.14	36	22	0.40	41
Silty clay loam	2.14	38	22	0.10	43
Sandy clay	2.11	36	25	0.52	38
Silty clay	2.12	41	27	0.06	46
Clay	2.10	42	30	0.22	38

1161

1162

1163

1164

1165

1166